

Displaced Higgs production in Type-III Seesaw at the LHC/FCC, MATHUSLA and Muon collider

Chandrima Sen,^a Priyotosh Bandyopadhyay,^b Saunak Dutta,^c Aleesha KT^d

^{a,b,c}*Indian Institute of Technology Hyderabad, Kandi, Sangareddy-502285, Telengana, India*

^c*SGTB Khalsa College, University of Delhi, New Delhi, India.*

^d*Department of Physical Sciences, Indian Institute of Science Education and Research Kolkata, Mohanpur, 741246, India*

E-mail: ph19resch11014@iith.ac.in , bpriyo@phy.iith.ac.in,
ph17resch11002@iith.ac.in, aleeshakt949@gmail.com

ABSTRACT: In this article, we explore the possibility of displaced Higgs production from the decays of the heavy fermions in the Type-III seesaw extension of the Standard Model at the LHC/FCC and the muon collider. The displaced heavy fermions and the Higgs boson can be traced back by measuring the displaced charged tracks of the charged leptons along with the b -jets. A very small Yukawa coupling can lead to two successive displaced decays which makes the phenomenology even more interesting. The prospects of the transverse and longitudinal displaced decay lengths are extensively studied in the context of the boost at the LHC/FCC. Due to the parton distribution function, the longitudinal boosts leads to larger displacement compared to the transverse one, which can reach MATHUSLA and beyond. The longitudinal measurements are indeed possible by the visible part of the finalstate, which captures the complete information about the longitudinal momenta. The comparative studies are made at the LHC/FCC with the centre of mass energies of 14, 27 and 100 TeV, respectively. A futuristic study of the muon collider where the collision happen in the centre of mass frame is analysed for centre of mass energies of 3.5, 14 and 30 TeV. Contrary to LHC/FCC, here the transverse momentum diverges, however, the maximum reach in both the direction are identical due to the constant total momentum in each collision. The reach of the Yukawa couplings and fermion masses are appraised for both the colliders. HL-LHC at 100 TeV can probe a mass of 5.8 TeV and a lowest Yukawa coupling of $\mathcal{O}(10^{-11})$.

Contents

1	Introduction	1
2	Type III Seesaw: The Model	3
3	Benchmark points and Displaced vertex	6
4	Setup for collider simulation	9
5	Simulations at the LHC/FCC	9
5.1	Kinematical distributions	9
5.2	Displaced decays at the CMS, ATLAS and MATHUSLA	14
5.3	Results	17
6	Simulation at the muon collider	24
6.1	Kinematical distributions	25
6.2	Boost effects at the muon collider	29
6.3	Displaced decays at the muon collider	30
6.4	Results	32
7	Reach plots in Yukawa versus mass plane	35
8	Conclusion	37

1 Introduction

Neutrinos are massless in Standard Model (SM), but observation of neutrino oscillation data [1, 2] needs neutrinos to be massive but very tiny. Explanation of tiny neutrino mass can be elucidated via Seesaw mechanisms, and one of such existing mechanism is Type-III [3–7], where the new beyond Standard Model (BSM) fermions are in spin one representation of $SU(2)$. There are numerous phenomenological studies at the LHC and other colliders on Type-III seesaw probing different aspects of the BSM scenarios [8–23] along with the generic displaced decay phenomenology [24]. The Type-III seesaw model has been studied considering electroweak vacuum stability [25], and limits on heavy fermion generation have been drawn for inverse Type-III scenario from the perturbativity of $SU(2)$ gauge coupling [26]. Recent searches of Type-III fermions at the LHC has put a lower limit on the mass of Type-III fermions as ~ 740 GeV [27–29] at 2σ level, which leaves the possibility of such heavy fermions around TeV along with the indirect bounds [30]. However, such bounds are obtained using prompt leptonic signature, which may reduce further in the case of displaced leptonic signature as some of the events will be missed by the detectors at the LHC.

The explanation of atmospheric neutrino mass required relatively small neutrino Yukawa couplings $\mathcal{O}(10^{-7})$ for $\mathcal{O}(100)$ GeV heavy neutrino mass scale. For solar neutrinos mass scale, the couplings will be one order of magnitude less. One or more neutrino Yukawa couplings can be even further small giving larger displaced decays, whereas the other one remains relatively large. The tiny neutrino Yukawa coupling can lead to the displaced production of the Higgs boson, which can be reconstructed via its dominant decay mode $b\bar{b}$. The displaced signature is clean from any background, and it can be used to constrain the Yukawa couplings. Such a scenario is explored in the context of supersymmetry while considering the decays of the scalar partners of the heavy neutrinos [31].

In this article, we initially explore the displaced Higgs production at the LHC/FCC with the centre of mass energies of 14, 27 and 100 TeV in the detectors CMS, ATLAS [32] and MATHUSLA [33–36]. MATHUSLA is a proposed detector with a 100 – 500 m range of displaced decay signature, which would be able to probe even smaller effective coupling in constraining or discovering new physics. However, the muon collider can open up new frontiers with energies of 3.5, 14 and 30 TeV as we propose the detectors for long lived particles.

In particular, we devote our analysis to including the boost effect in the transverse and the longitudinal directions. At the LHC, colliding parton momenta are unknown and governed by the parton distribution functions. This causes a boosted system mostly in the longitudinal directions. If the BSM particle decays into a complete visible mode, we can measure the momenta and the exact displaced decay length of such particles. MATHUSLA detector will be only on one side of the LHC detectors, thus asymmetric in the z -axis. While the transverse direction is symmetric, the amount of boost is negligible compared to the longitudinal one. Additionally, if there is only one missing particle in the final state the momentum can be reconstructed as the total transverse momentum is zero at any given point. Thus the momentum of the actual BSM particle can be constructed, enabling us to estimate the boosted decay length of that BSM particle. A comparative study for transverse and longitudinal decay lengths are given for CMS, ATLAS and MATHUSLA for the centre of mass energies of 14, 27 and 100 TeV at the LHC/FCC and model independent limits on the parameter space based on these collider searches are derived.

Recently muon collider [37–41] is receiving lots of attention for studying various BSM scenarios due to the precision measurements, centre of mass frame, no initial state QCD radiation, etc [42–54]. The long lived particles can also be explored at the muon collider, where we proposed such displaced vertex measurement facility, which can be instrumental in exploring some of these BSM scenarios. As opposed to LHC/FCC, in a muon collider, the total momentum is constant for each collision since it happens in the centre of mass frame. One interesting fact is that the transverse momentum for the Type-III fermion diverges perpendicular to the beam axis, i.e. pseudorapidity goes to zero. This results in slight enhancement of the number of events for higher transverse decay length compared to longitudinal ones. The highest reach of the decay length is constrained by the maximum momentum, which in this case is the net momentum, and thus for both scenarios, maximum decay length will be identical. The analysis has been carried out for centre of mass energies of 3.5, 14 and 30 TeV with 1000, 10000 and 30000 fb^{-1} and limits on mass and coupling

are drawn.

This article is organised as follows. In [section 2](#), we describe the model and the decay modes. In [section 3](#), we discuss the allowed parameter space and choose our benchmark points for the displaced vertex. The collider setups are discussed in [section 4](#). The simulations at the LHC/FCC, including the kinematics, displaced vertex and results are given in [section 5](#). Similarly, for the muon collider, these are detailed in [section 6](#). The coupling versus mass regions that can be explored are summarised in [section 7](#) and finally, we present our conclusions in [section 8](#).

2 Type III Seesaw: The Model

The new $SU(2)$ triplet fermions (N) with hypercharge (Y) zero can be added to the SM Lagrangian with the addition of the following terms as given in [Equation 2.1](#)

$$\mathcal{L}_N = \text{Tr}(\bar{N}\not{D}N) - \frac{1}{4}M_N \text{Tr}[\bar{N}N] - Y_N (\tilde{\phi}^\dagger \bar{N}L + \bar{L}N\tilde{\phi}), \quad (2.1)$$

where $\phi = \begin{pmatrix} G^\pm \\ \frac{1}{\sqrt{2}}(h + v + iG^0) \end{pmatrix}$ is the Higgs doublet in Standard Model and, $L = \begin{pmatrix} \nu_\ell \\ \ell \end{pmatrix}$ is the left handed lepton doublet. Here G^\pm and G^0 are charged and neutral Goldstone bosons, h is the physical Higgs boson and v is the vacuum expectation value (vev) which generates the mass for the SM particles. In [Equation 2.1](#), we use $\tilde{\phi} = i\sigma^2\phi^*$ and the N_i are represented by [Equation 2.2](#). N_i has one pair of charged fermion (N_i^\pm) and one neutral component (N_i^0) for each generation i ($i = 1, 2, 3$) respectively.

$$N_i = \begin{pmatrix} N_i^0 & \sqrt{2}N_i^+ \\ \sqrt{2}N_i^- & -N_i^0 \end{pmatrix} \quad (i = 1, 2, 3) \quad (2.2)$$

For the simplicity of the collider study, we consider the N_i in diagonal basis along with the Y_{N_i} . As the Higgs boson gets vev, i.e. $\langle \phi \rangle = \frac{v}{\sqrt{2}}$, the light neutrino mass is generated, which is scaled by the Type-III fermion mass as given below

$$m_{ij}^\nu = \frac{Y_{N_i}Y_{N_j}v^2}{2M_N}. \quad (2.3)$$

At the LHC, associated N^0N^\pm can be produced via W^\pm boson exchange as well as the pair of N^\pm via photon and Z boson which can be seen from [Figure 1\(a\), \(b\)](#). Unlike at the LHC, in the muon collider, N^0N^\pm cannot be produced.

The hard scattering cross-sections can be calculated as

$$\frac{d\sigma}{d\hat{s}^2} = \sum_q \int dx \int dy f_q(x) f_{\bar{q}}(y) \frac{d\hat{\sigma}}{d\hat{s}^2}, \quad (2.4)$$

where we need to use the parton distribution functions $f_q(x)$ at the LHC/FCC. For this article, we have used NNPDF23_lo_as_0130_qed [\[55\]](#). The partonic differential distribution of the cross-section can be written as

$$\frac{d\hat{\sigma}}{d\cos\theta} = \frac{V_L^2 + V_R^2}{64\pi} \beta N_c (4M_N^2 + \hat{s} - \beta^2 \hat{s} \cos^2 \theta), \quad (2.5)$$

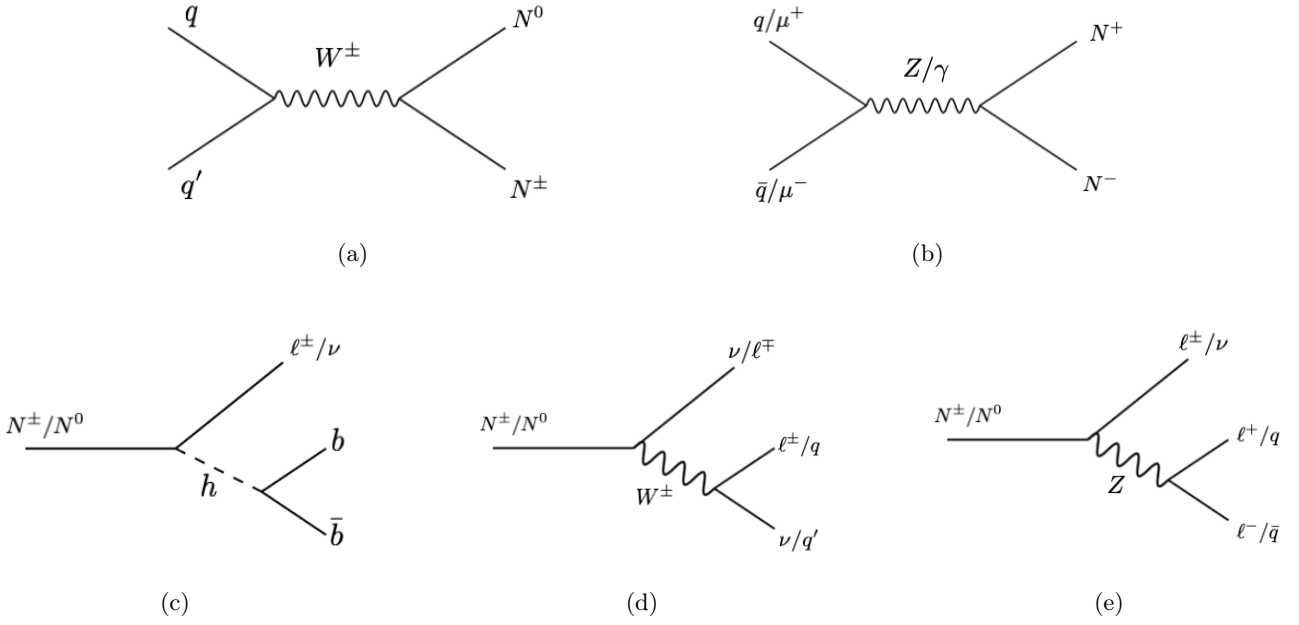


Figure 1. Feynman diagrams of the production processes of Type-III fermions N^0 and N^\pm . (a) shows the associated production at the LHC/FCC and (b) depicts the pair production of N^\pm at the LHC/FCC and the muon collider. The decay of N^0 and N^\pm to Higgs boson and SM gauge bosons are shown in (c), (d) and (e).

where $N_c = 3$ for quarks (=1 for leptons), $\beta = \sqrt{1 - \frac{4M_N^2}{\hat{s}}}$ [56] is the velocity of Type-III fermions ($0 \leq \beta \leq 1$) and

$$V_A = \frac{Q_f e^2}{\hat{s}} + \frac{g_A^f g_2^2}{\hat{s} - M_Z^2} \quad \text{for } q\bar{q}/\ell^+\ell^- \rightarrow N^+N^- \quad (2.6)$$

$$V_A = \frac{g_2^2}{\hat{s} - M_W^2} \frac{\delta_{AL}}{\sqrt{2}} \quad \text{for } q\bar{q}' \rightarrow N^0N^\pm. \quad (2.7)$$

Here the Z coupling for the fermion f is given by $g_A^f = T_3 - s_W^2 Q_f$, where Q_f is the electric charge factor corresponding to quarks or leptons and A corresponds to the chirality $\{L, R\}$.

Due to the vev of the Higgs bosons, such heavy fermions decays to SM particles like gauge bosons, Higgs boson and fermions. Figure 1 shows the decay channels of N^\pm and N^0 , which further decays to SM particles, where we only focus on $h \rightarrow b\bar{b}$ for our study. The two-body decay widths for N^\pm and N^0 are proportional to Y_N^2 [5] and are given by

$$\Gamma(N^0 \rightarrow \nu_\ell h) = \Gamma(N^0 \rightarrow \bar{\nu}_\ell h) = \frac{1}{8} \frac{Y_N^2 M_N}{8\pi} \left(1 - \frac{M_h^2}{M_N^2}\right)^2, \quad (2.8)$$

$$\Gamma(N^0 \rightarrow \nu_\ell Z) = \Gamma(N^0 \rightarrow \bar{\nu}_\ell Z) = \frac{1}{8} \frac{Y_N^2 M_N}{8\pi} \left(1 - \frac{M_Z^2}{M_N^2}\right)^2 \left(1 + 2 \frac{M_Z^2}{M_N^2}\right), \quad (2.9)$$

$$\Gamma(N^0 \rightarrow W^+ \ell^-) = \Gamma(N^0 \rightarrow W^- \ell^+) = \frac{1}{4} \frac{Y_N^2 M_N}{8\pi} \left(1 - \frac{M_W^2}{M_N^2}\right)^2 \left(1 + 2 \frac{M_W^2}{M_N^2}\right) \quad (2.10)$$

and

$$\Gamma(N^\pm \rightarrow \ell^\pm h) = \frac{1}{4} \frac{Y_N^2 M_N}{8\pi} \left(1 - \frac{M_h^2}{M_N^2}\right)^2, \quad (2.11)$$

$$\Gamma(N^\pm \rightarrow \ell^\pm Z) = \frac{1}{4} \frac{Y_N^2 M_N}{8\pi} \left(1 - \frac{M_Z^2}{M_N^2}\right)^2 \left(1 + 2 \frac{M_Z^2}{M_N^2}\right), \quad (2.12)$$

$$\Gamma(N^\pm \rightarrow \nu_\ell W^\pm) = \frac{1}{2} \frac{Y_N^2 M_N}{8\pi} \left(1 - \frac{M_W^2}{M_N^2}\right)^2 \left(1 + 2 \frac{M_W^2}{M_N^2}\right), \quad (2.13)$$

respectively, where we drop the generation index i for simplicity.

There are another decay modes possible considering the loop generated mass of N^\pm and N^0 , which gives a mass splitting of $\Delta M = \mathcal{O}(166)$ MeV [56]. It opens up the following decays with the widths given by

$$\Gamma(N^\pm \rightarrow N^0 \pi^\pm) = \frac{2G_F^2 V_{ud}^2 \Delta M^3 f_\pi^2}{\pi} \sqrt{1 - \frac{m_\pi^2}{\Delta M^2}}, \quad (2.14)$$

$$\Gamma(N^\pm \rightarrow N^0 e^\pm \nu_e) = \frac{2G_F^2 \Delta M^5}{15\pi^3}, \quad (2.15)$$

$$\Gamma(N^\pm \rightarrow N^0 \mu^\pm \nu_\mu) = 0.12 \Gamma(N^\pm \rightarrow N^0 e^\pm \nu_e), \quad (2.16)$$

where $f_\pi = 130.5$ MeV is the pion form factor, G_F is the Fermi constant and V_{ud} is the CKM mixing matrix.

For $Y_N = 5 \times 10^{-7}$ and $M_N = 1$ TeV, $\mathcal{B}(N^\pm \rightarrow N^0 \pi^\pm) \sim 0.25\%$ and has negligible effect on our collider study for this choice of Yukawa. Such behaviour can be visible from Figure 2(a) with respect to M_N . However, for even lower choices of Y_N i.e. for 10^{-8} , 5×10^{-10} , the decay of $N^\pm \rightarrow N^0 \pi^\pm$ becomes dominant with branching ratios of 84% and 100% respectively for $M_N = 1$ TeV. So for these lower Y_N values, we see a displacement of N^\pm to π^\pm , N^0 , which is of the order of cm before the N^0 decay gives another recoil. The total displaced decay length will thus depend on both the decays of N^\pm and N^0 as can be seen from the schematic diagram of Figure 3.

For the collider study we follow the model independent approach keeping Yukawa couplings which can be very low $\sim 10^{-10}$, almost a free parameter, probing the displaced vertices at CMS, ATLAS, MATHUSLA and muon collider. The constrained neutrino mass and mixing matrix would lie in some region of the parameter space [20, 57] which can also include one massless neutrino at the tree-level.

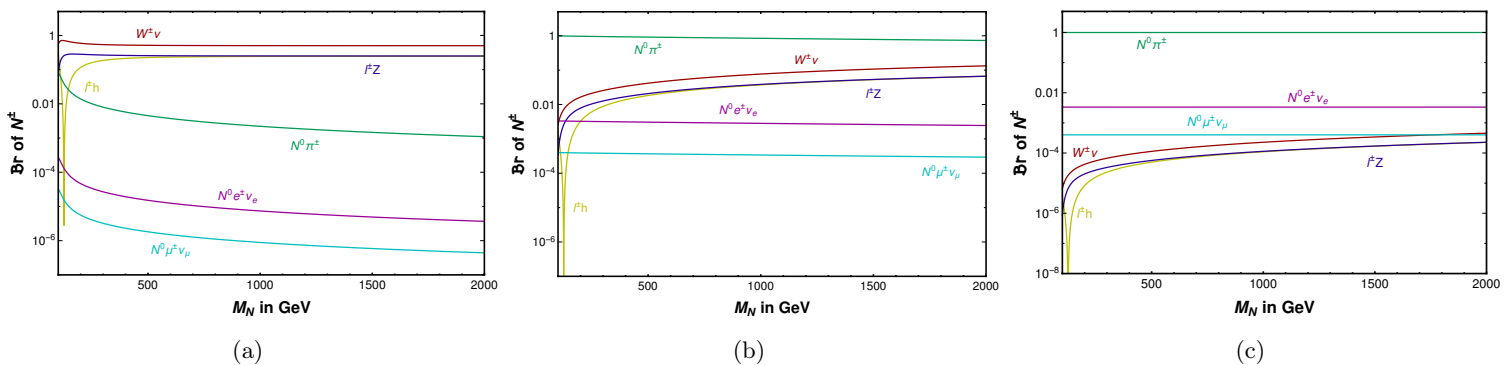


Figure 2. Charged $SU(2)_L$ triplet heavy fermion branching ratios to different decay channels as function of the triplet mass. Yukawa couplings $Y_N = 5 \times 10^{-7}$, 1×10^{-8} , 5×10^{-10} are for (a), (b) and (c), respectively.

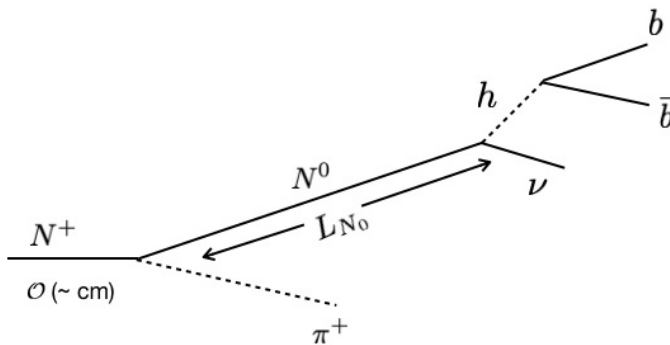


Figure 3. Schematic diagram of $N^\pm \rightarrow N^0\pi^\pm$ and $N^0 \rightarrow h\nu$ decays.

3 Benchmark points and Displaced vertex

The recent collider searches at CMS [27, 29] and ATLAS [28] have put a lower bound of 740 GeV at 2σ level, on the Type-III fermion mass. This prompts us to choose masses of 750, 1000 and 1500 GeV as BP1, BP2, BP3, respectively for the collider study as listed in Table 1. Table 1 describes the branching fractions of the neutral heavy fermion (N_i^0) to $W^\pm\ell^\mp$, $Z\nu$ and $h\nu$, and charged heavy fermions (N_i^\pm) to $W^\pm\nu$, $Z\ell^\pm$ and $h\ell^\pm$, which are around 2:1:1 for all the benchmark points. Here N_i^\pm decay branching fractions are for $Y_N = 5 \times 10^7$ and for other Yukawa couplings we incorporate the decay branching fractions appropriately. The Higgs boson is the SM like one with a mass around 125.5 GeV, which dominantly decays to $b\bar{b}$.

The production cross-sections in both LHC/FCC with the centre of mass energies of 14, 27 and 100 TeV are given in Table 2, where NNPDF23_lo_as_0130_qed [55] is used as the parton distribution function. It is interesting to see the enhancement of the cross-sections as we increase the centre of mass energy at the LHC/FCC. Due to the parton distribution

Modes	BP1	BP2	BP3
	$M_N = 750 \text{ GeV}$	$M_N = 1000 \text{ GeV}$	$M_N = 1500 \text{ GeV}$
$N_i^0 \rightarrow h \bar{\nu}_i^{(-)}$	24.1	24.4	24.7
$N_i^0 \rightarrow Z \bar{\nu}_i^{(-)}$	25.3	25.2	25.1
$N_i^0 \rightarrow W^\pm l_i^\mp$	50.6	50.4	50.2
$N_i^\pm \rightarrow h l_i^\pm$	24.0	24.4	24.7
$N_i^\pm \rightarrow Z l_i^\pm$	25.3	25.2	25.1
$N_i^\pm \rightarrow W^\pm \bar{\nu}_i^{(-)}$	50.7	50.4	50.2

Table 1. Masses of the Type-III fermions (M_N) and their branching ratios (in %) for the different decay modes of N_i^0 and N_i^\pm , where i ($= 1, 2, 3$) is the generation index. Here N_i^\pm decay branching fractions are for $Y_N = 5 \times 10^7$.

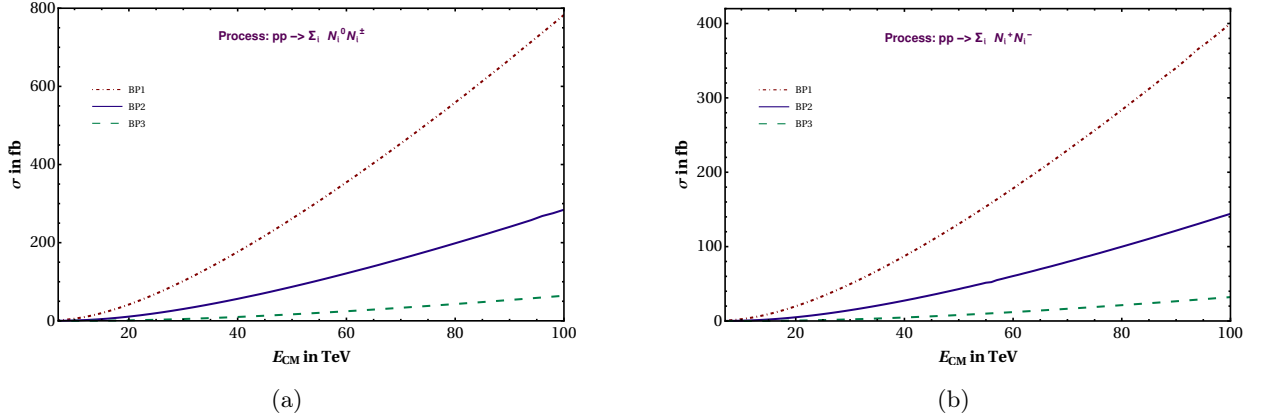


Figure 4. Cross-section (in fb) as a function of centre of mass energy (E_{CM}) for the benchmark points at the LHC for the processes $pp \rightarrow \Sigma_i N_i^0 N_i^\pm$ (a) and $pp \rightarrow \Sigma_i N_i^+ N_i^-$ (b), where i ($= 1, 2, 3$) is the generation index.

function we always find the on-shell production even at higher energies, contrary to the muon collider. Unlike LHC/FCC, in muon collider, we cannot produce $N_i^\pm N_i^0$ and we rely only on the pair production of $N_i^\pm N_i^\mp$ as we present the cross-sections in Table 12 with the centre of mass energies of 3.5, 14 and 30 TeV for the benchmark points. Due to $Y = 0$ nature, the pair production of $T_3 = 0$ component of $SU(2)$, i.e. N_i^0 is not possible in both of the colliders. However, via N^\pm decay, the pair production of N^0 is possible for lower Yukawa couplings as $N^\pm \rightarrow N^0 \pi^\pm$ decay mode gets dominant.

The chosen benchmark points in Table 1, can give rise to displaced decays with the rest

Benchmark points	Cross-sections (in fb) with the E_{CM}					
	14 TeV		27 TeV		100 TeV	
	$\Sigma_i N_i^0 N_i^\pm$	$\Sigma_i N_i^+ N_i^-$	$\Sigma_i N_i^0 N_i^\pm$	$\Sigma_i N_i^+ N_i^-$	$\Sigma_i N_i^0 N_i^\pm$	$\Sigma_i N_i^+ N_i^-$
BP1	16.2	7.5	81.9	39.7	783.3	400.2
BP2	3.4	1.6	23.6	11.2	284.1	144.1
BP3	0.3	0.1	3.4	1.6	64.3	32.1

Table 2. Inclusive production cross-sections (in fb) of the processes $pp \rightarrow \Sigma_i N_i^0 N_i^\pm$ and $pp \rightarrow \Sigma_i N_i^+ N_i^-$, for the benchmark points at the LHC for 14 TeV, 27 TeV and 100 TeV centre of mass energies, where i ($= 1, 2, 3$) is the generation index.

M_N \backslash Y_N	Rest Mass Decay Length		
	5×10^{-7}	1×10^{-8}	5×10^{-10}
750 GeV	0.03 mm	6.80 cm	27.21 m
1.0 TeV	0.02 mm	5.06 cm	20.26 m
1.5 TeV	0.01 mm	3.36 cm	13.42 m

Table 3. Rest mass decay length of N^0 for the chosen benchmark points for $Y_N = 5 \times 10^{-7}$.

mass decay lengths for N^0 ranging from mm to hundreds of meters for neutrino Yukawa couplings $Y_N \sim 10^{-7} - 10^{-10}$ as shown in Table 3. However, for N^\pm the decay length is governed by Y_N and for $Y_N \sim 10^{-7}$ giving rise to similar decay length of N^0 . For lower Y_N , i.e. $10^{-8} - 10^{-10}$, it is dominated by $N^\pm \rightarrow N^0 \pi^\pm$ and displaced decay in such case is around cm. However, such rest mass decay lengths will be further affected due to the probability distribution of the decay and also because of the boost effect in the finalstates. In particular, we focus on the effect of the latter, where LHC/FCC and muon collider behave differently. For this purpose, we perform a detailed simulation by PYTHIA8 [58], which takes care of the boost effect and the decay distributions, etc. We see in the following sections that in the case of LHC, longitudinal boost plays a major role in enhancing the decay lengths and at the muon collider, the transverse momenta diverges affecting the corresponding decay lengths. The collider setup is described below before presenting the relevant kinematical distributions and analysis.

4 Setup for collider simulation

The model has been implemented in SARAH 4.13.0[59] to generate the model files for CalcHEP_3.8.7[60]. The cross-sections at tree-level and event generation are performed in CalcHEP with the parton distribution function NNPDF23_1o_as_0130_qed[55]. The events are then analysed in PYTHIA8 [58] with initial, final state radiations and subsequent hadronisation. Such hadrons are then fed to Fastjet_3.2.3 [59] for jet formation with the following specifications.

- Calorimeter coverage: $|\eta| < 2.5$.
- Jet clustering is done by ANTI-KT algorithm with jet Radius parameter, $R = 0.5$.
- Minimum transverse momentum of each jet: $p_{T,min}^{jet} = 20.0$ GeV; jets are p_T -ordered.
- No hard leptons are inside the jets.
- Minimum transverse momentum cut for each detected lepton: $p_{T,min}^{lep} = 20.0$ GeV.
- Detected leptons are hadronically clean, which implies hadronic activity within a cone of $\Delta R < 0.3$ around each lepton is less than 15% of the leptonic transverse momentum, *i.e.* $p_T^{had} < 0.15 p_T^{lep}$ within the cone.
- Leptons are distinctly registered from the jets produced with an isolation cut $\Delta R_{lj} > 0.4$.

We reconstruct the Higgs bosons via $b\bar{b}$ mode, where the b -jets are tagged via the secondary vertex reconstruction with b -jet tagging efficiency of maximum 85% [61, 62].

5 Simulations at the LHC/FCC

In this section, we describe all the crucial kinematical distributions leading to displaced Higgs reconstructions. The effect of heavy fermion mass, Yukawa and the centre of mass energy of the collider are explored in detail while projecting the number of events at the LHC/FCC and MATHUSLA.

5.1 Kinematical distributions

We describe the lepton (μ, e) multiplicity distributions at the LHC/FCC in Figure 5 with three different centre of mass energies for the second benchmark point (BP2). The production processes $N^0 N^\pm$ and $N^\pm N^\mp$ are depicted in Figure 5(a) and (b), respectively. After imposing the isolation criteria, although the distribution peaks around one, the lepton multiplicity reaches till four.

Figure 6 demonstrates the lepton p_T distributions for BP2. Figure 6(a) corresponds to the production mode of $pp \rightarrow N^+ N^-$, where $N^\pm \rightarrow h e^\pm$ is kept at 100% and jet-lepton isolation is not demanded. Indeed, both the leptons (red and green curves) coming from N^\pm decays have identical p_T distributions. The effect of jet-lepton isolation can be observed

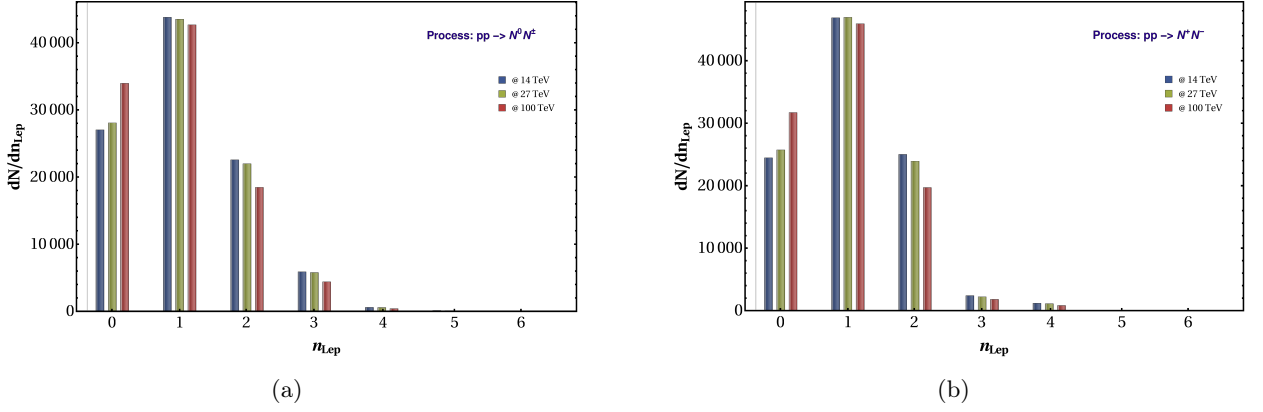


Figure 5. Multiplicity (n_{Lep}) distributions of the charged leptons for the process $pp \rightarrow N^0 N^\pm$ (a) and $pp \rightarrow N^+ N^-$ (b) at the three different centre of mass energies of 14 TeV, 27 TeV and 100 TeV for $M_N = 1$ TeV (BP2) and $Y_N = 5 \times 10^{-7}$.

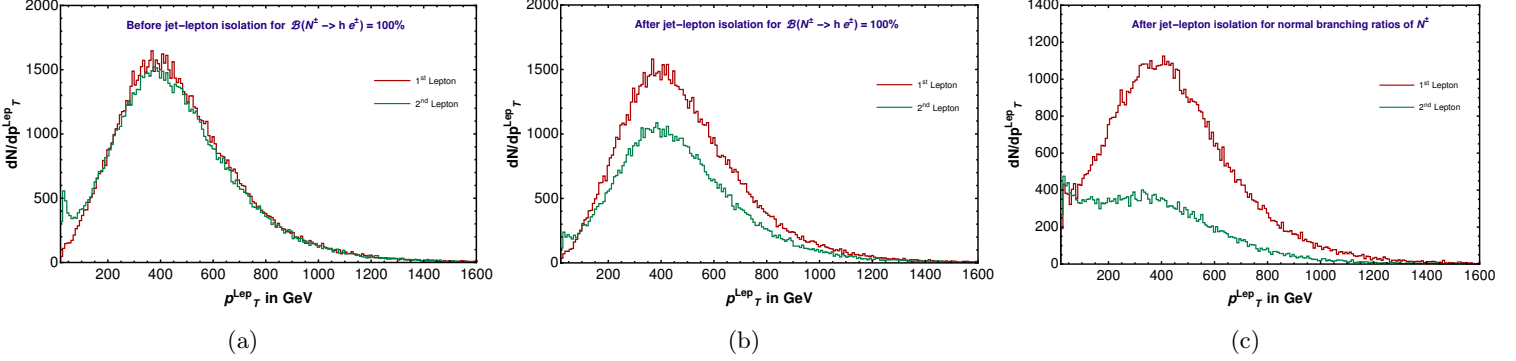


Figure 6. The transverse momentum (p_T) distributions of charged leptons (1^{st} and 2^{nd}) at the LHC for the process $pp \rightarrow N^+ N^-$ with $M_N = 1$ TeV, $Y_N = 5 \times 10^{-7}$ and center of mass energy 14 TeV. (a) and (b) represent the distributions of two leptons for pre and post jet-lepton isolation, respectively for $\mathcal{B}(N^\pm \rightarrow h e^\pm) = 100\%$. (c) describes the scenario for the isolated leptons obeying the branching ratio of BP2.

in [Figure 6\(b\)](#). Though the distributions are identical, the isolation cuts are responsible for the relatively low yield of the second lepton. Finally, we have the distribution in [Figure 6\(c\)](#), where the branching fractions of the decay mode are kept as in BP2 for $Y_N = 5 \times 10^{-7}$. In this case, the second leptons can be from the gauge boson decays, thus lower in p_T (green curve).

[Figure 7](#) illustrates the jet multiplicity distributions for BP2 for the centre of mass energies of 14 TeV, 27 TeV and 100 TeV. [Figure 7\(a\)](#) and (b) represents the process of $pp \rightarrow N^0 N^\pm$ and $pp \rightarrow N^+ N^-$, respectively. The distributions in blue, olive green and red corresponds to centre of mass energies of 14, 27 and 100 TeV, respectively. In both cases, the multiplicity peak around three and ISR/FSR jets increase as we go for the higher centre

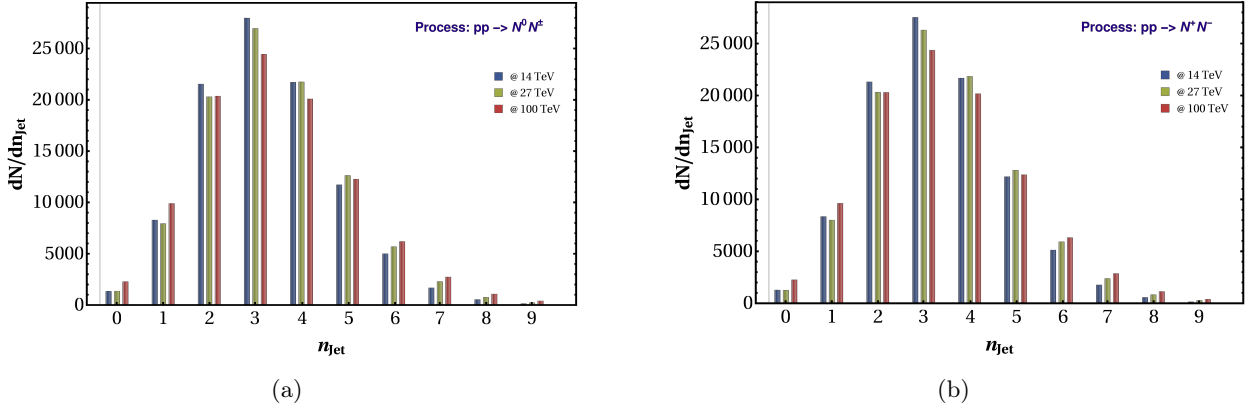


Figure 7. Jet multiplicity (n_{Jet}) distributions for the process $pp \rightarrow N^0 N^\pm$ (a) and $pp \rightarrow N^+ N^-$ (b) at $E_{CM} = 14$ TeV, 27 TeV and 100 TeV for $Y_N = 5 \times 10^{-7}$ and $M_N = 1$ TeV (BP2).

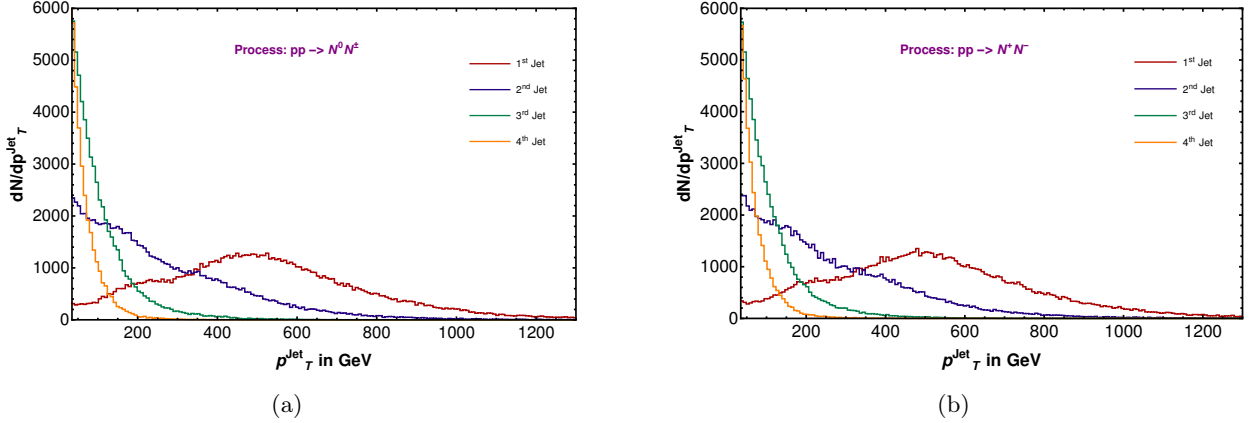


Figure 8. The transverse momentum (p_T) distributions of the first four p_T ordered jets at the LHC for the process $pp \rightarrow N^0 N^\pm$ (a) and $pp \rightarrow N^+ N^-$ (b) with $M_N = 1$ TeV (BP2), $Y_N = 5 \times 10^{-7}$ and center of mass energy of 14 TeV.

of mass energy.

In Figure 8, we present the jet p_T distributions of the first four p_T ordered jets for BP2 at the centre of mass energy of 14 TeV. The leading jet (in red) peaks around $\frac{M_N}{2}$ as the two jets coming from the gauge bosons or Higgs boson become collinear due to large boost effect and combine as single jet. The second jet (in blue) either comes from the gauge boson decay or the other BSM fermion and is relatively harder. The third and fourth jets (in green and orange) which come from the decay of gauge bosons are of lower p_T .

Figure 9 (a) and (b) describes the multiplicity distributions for the b -jets coming from the Higgs boson decays for the production modes of $pp \rightarrow N^0 N^\pm$ and $pp \rightarrow N^+ N^-$, respectively at three different centre of mass energies, 14 TeV, 27 TeV and 100 TeV with $M_N = 1$ TeV (BP2) and $Y_N = 5 \times 10^{-7}$. The Higgs boson and the Z boson coming from

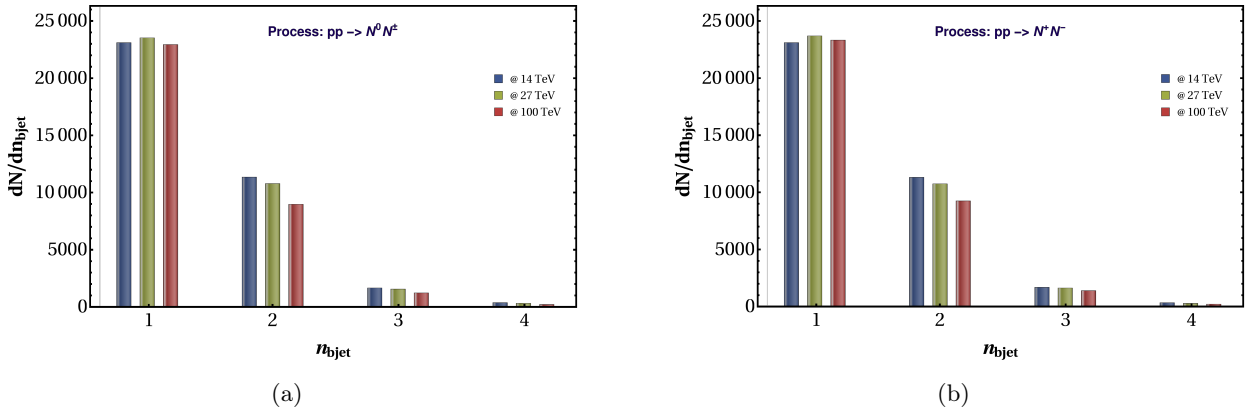


Figure 9. b -jet multiplicity ($n_{b\text{jet}}$) distributions for the process (a) $pp \rightarrow N^0 N^\pm$ and (b) $pp \rightarrow N^+ N^-$ at $E_{CM} = 14$ TeV, 27 TeV and 100 TeV for $M_N = 1$ TeV (BP2) and $Y_N = 5 \times 10^{-7}$.

$N^{\pm(0)}$ are the two sources of such b -jets. The unwanted background b -jet coming from Z decay can be eliminated via the reconstruction of di- b -jet invariant mass distributions. The b -jets coming from the Higgs bosons or Z boson decays can be traced back by reconstructing their invariant mass distributions. The b -jets are tagged via the secondary vertex reconstitution of the b hadrons associated with the jets. We follow the b -jet tagging efficiency of CMS with a maximum of 85% [61, 62]. The multiplicity of b -jets can go up to four as they come from both the Higgs bosons decays.

At the LHC, we do not know the centre of mass frame of the collision due to unknown longitudinal boost governed by the parton distribution functions which dictates the momentum sharing of the colliding partons. The sharing of the colliding energies of the quarks in this case also varies with centre of mass energies. If we evaluate the heavy fermion decays in complete visible mode i.e. $N^\pm \rightarrow h\ell^\pm$, the reconstruction of the heavy fermion momentum is possible and allows us to measure both p_T and p_z of N^\pm . This further enables us to determine the longitudinal decay length, in addition to the transverse decay length. On the contrary, it is not possible to reconstruct the total momentum of the neutrino coming from $N^0 \rightarrow h\nu$ decay due to the lack of knowledge of the longitudinal boost of the partonic system. However, as the net transverse momentum is zero, for $pp \rightarrow N^0 N^\pm \rightarrow h h \ell^\pm \nu$, where only a single neutrino contributes towards missing momentum, we can easily calculate the transverse missing momentum as neutrino p_T . Thus, for $pp \rightarrow N^0 N^\pm$, only transverse momentum and consequently the transverse decay length can be calculated, whereas, for $pp \rightarrow N^+ N^-$, we can compute the displaced decay length in both transverse and longitudinal direction. Such conclusion is however, bound to change as we move towards lower Yukawa coupling i.e., $Y_N \leq 10^{-8}$ where, $N^\pm \rightarrow \pi^\pm N^0$ becomes dominant and multiple neutrinos coming from pion and other decays can smear the invariant mass distributions.

Another intriguing feature that we observe is that the enhanced displaced decay length in the longitudinal direction due to the large longitudinal boost compared to the transverse one. This can be inferred from Figure 10 which shows the comparison between transverse

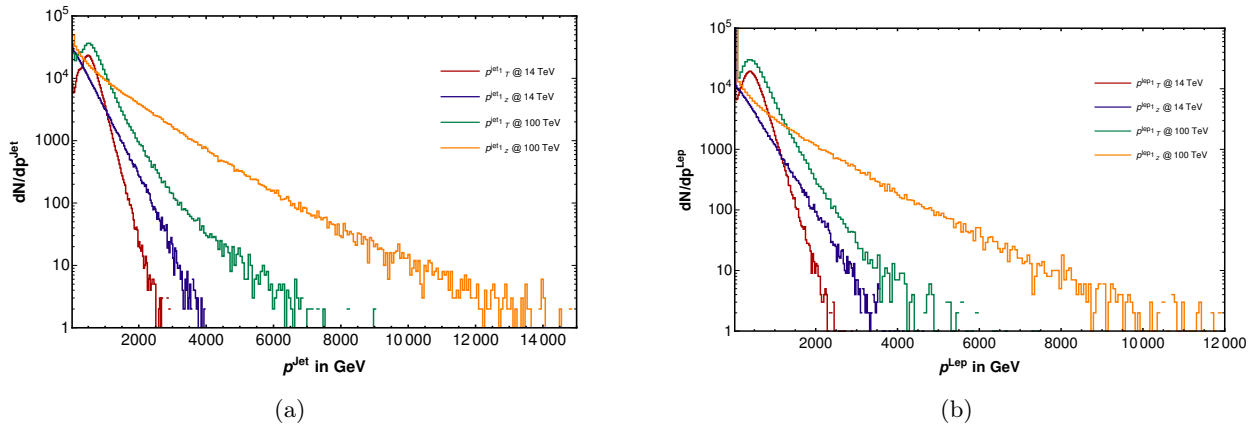


Figure 10. The transverse and longitudinal momenta distributions of the leading jet (a) and the first lepton (b) for the process $pp \rightarrow N^+ N^-$, with $M_N = 1$ TeV (BP2), $Y_N = 5 \times 10^{-7}$ and center of mass energies of 14 TeV and 100 TeV at the LHC.

Centre of mass energy	% of events for $P_z^{\text{jet}} > P_c^{\text{jet}}$		
	BP1	BP2	BP3
14 TeV	12.3%	8.4%	3.9%
27 TeV	21.0%	18.9%	11.9%
100 TeV	31.8%	31.3%	29.6%

Table 4. The percentage of events for $P_z^{\text{jet}} > P_c^{\text{jet}}$ distribution for the benchmark points at centre of mass of energies of 14, 27 and 100 TeV, where P_c^{jet} is the point of cross-over for P_z^{jet} and P_T^{jet} distributions as shown in Figure 10.

and longitudinal momentum of the jets and leptons at 14 TeV and 100 TeV for BP2 with $Y_N = 5 \times 10^{-7}$. Figure 10(a) depicts the comparison between p_T^j and $|p_z^j|$ at the centre of mass energies of 14 TeV and 100 TeV. In case of 14 TeV, the longitudinal momentum of the jet goes till 3.8 TeV as compared to 2.5 TeV of p_T^j and the cross-over of the two distributions happen around 1.3 TeV. Similarly, at 100 TeV, p_T^j reaches up to 7.5 TeV, while p_z^j reaches till 14 TeV with a cross-over around 1.5 TeV. Certainly, the extra boost in the longitudinal direction can further push the displaced decay compared to the transverse one. In Table 4 we see the number of events in percentage where $P_z^{\text{jet}} > P_c^{\text{jet}}$ and P_c^{jet} is the cross-over point of p_z and p_T as can be seen from Figure 10(a). It is evident that as we increase the centre of mass energy, the longitudinal boost increases more and thus events for which P_z^{jet} is greater than P_c^{jet} can be around 30% for 100 TeV centre of mass energy. Such effect can

be seen in the corresponding displaced decay lengths as we discuss them next.

Similarly Figure 10(b) depicts comparison between the charged lepton momentum distributions for BP2 at the centre of mass energies of 14 and 100 TeV. We can see similar effect as the jet momentum distributions in Figure 10(a). The longitudinal momentum is boosted as compared to the transverse one. In the following subsection, we examine both the transverse and the longitudinal displaced decays along with their reaches at CMS, ATLAS and MATHUSLA.

5.2 Displaced decays at the CMS, ATLAS and MATHUSLA

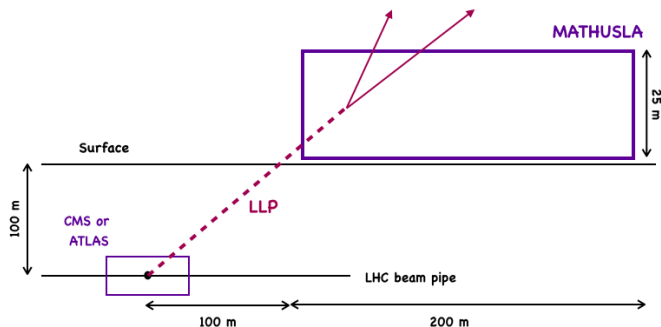


Figure 11. Schematic diagram of the MATHUSLA detector [35].

In this subsection, we study the distributions of the transverse and longitudinal decay lengths of N^\pm for three different centre of mass energies 14, 27 and 100 TeV, respectively for the benchmark points with three different Yukawa couplings. The displaced decays can be detected either in CMS, ATLAS or in a new proposed detector called MATHUSLA. CMS and ATLAS have transverse and longitudinal ranges of 7.5, 12.5 and 22, 44 meter [63, 64] respectively. However, the new proposed detector MATHUSLA is around 100 m from the CMS or ATLAS in the beam axis as well as in the transverse direction [33, 35] as shown in Figure 11. The length of the detector is 200 m with height of 25 m which give extra reach for the particle with late decay. In the next few paragraphs, we show how different benchmark points pan out in different detectors. The choices of Yukawa here are motivated from the collider searches of the different displaced decays and any further constraint would restrict the parameter points that we are interested in [20, 57].

In Figure 12, we show the total transverse displaced decays when N^\pm are pair produced for the benchmark points. We have used three panels for the centre of mass energies of 14 TeV (a, b, c), 27 TeV (d, e, f) and 100 TeV (g, h, i). The first column (a, d, g) describes the the Yukawa coupling satisfying the atmospheric neutrino mass scale corresponding to $M_N = \mathcal{O}(100)$ GeV, i.e. $Y_N = 5 \times 10^{-7}$. Here, N^\pm dominantly decays to SM particles i.e. $h\ell^\pm$, $Z\ell^\pm$, $W^\pm\nu$ and thus has one recoil after the first displacement. If we move further lower in Yukawa coupling i.e., $Y_N \leq 10^{-8}$ the $N^\pm \rightarrow \pi^\pm N^0$ decay modes becomes dominant and the first displacement happens in around cm and remains almost unchanged for all lower

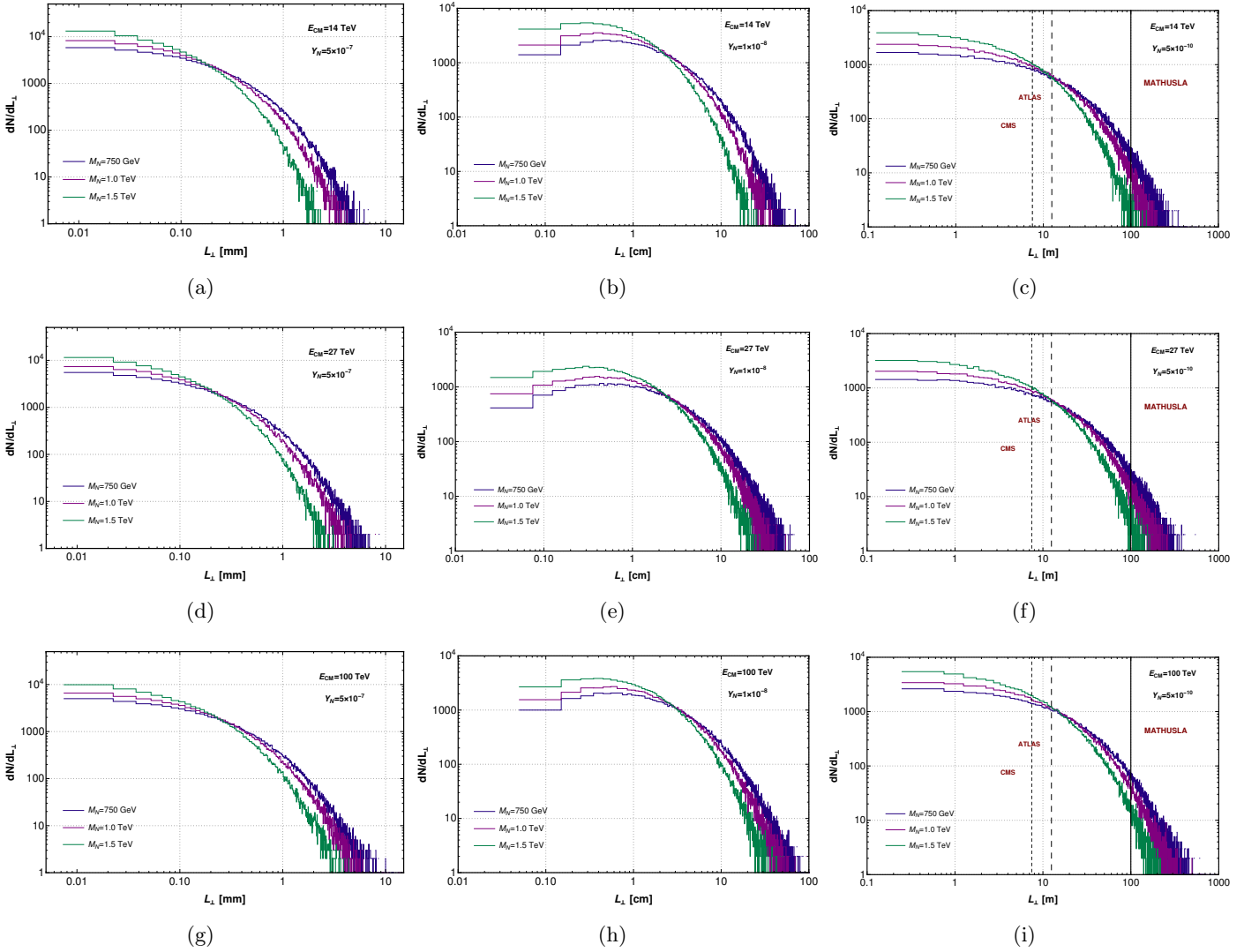


Figure 12. Displaced total transverse decay length (L_{\perp}) distributions for the N^{\pm} , coming from the pair productions at the LHC with the centre of mass energies 14 TeV (a, b, c), 27 TeV (d, e, f) and 100 TeV (g, h, i) for the benchmark points. Yukawa couplings $Y_N = 5 \times 10^{-7}$, 1×10^{-8} , respectively are used for atmospheric (a, d, g) and solar (b, e, h) neutrino mass scales for $\mathcal{O}(100)$ GeV Type-III fermion mass, whereas the third column (c, f, i) depicts $Y_N = 5 \times 10^{-10}$, for higher reach. The dotted-dashed and dashed line indicates the upper limit of CMS and ATLAS, respectively. The solid black line denotes the lower limit of MATHUSLA.

Yukawa couplings. N^0 thus produced will further give displaced decays depending on the Yukawa couplings. In Figure 12 (b, e, h) we illustrate the total displaced decay lengths including first and second recoils for the Solar neutrino mass scale i.e., $Y_N = 1 \times 10^{-8}$ for $M_N = \mathcal{O}(100)$ GeV. The total decay lengths corresponding to the Yukawa coupling of 5×10^{-10} for the benchmark points are illustrated in (c, f, i) which gives rise to decay lengths in the MATHUSLA range (≥ 100 m). It is apparent that, as the centre of mass energy

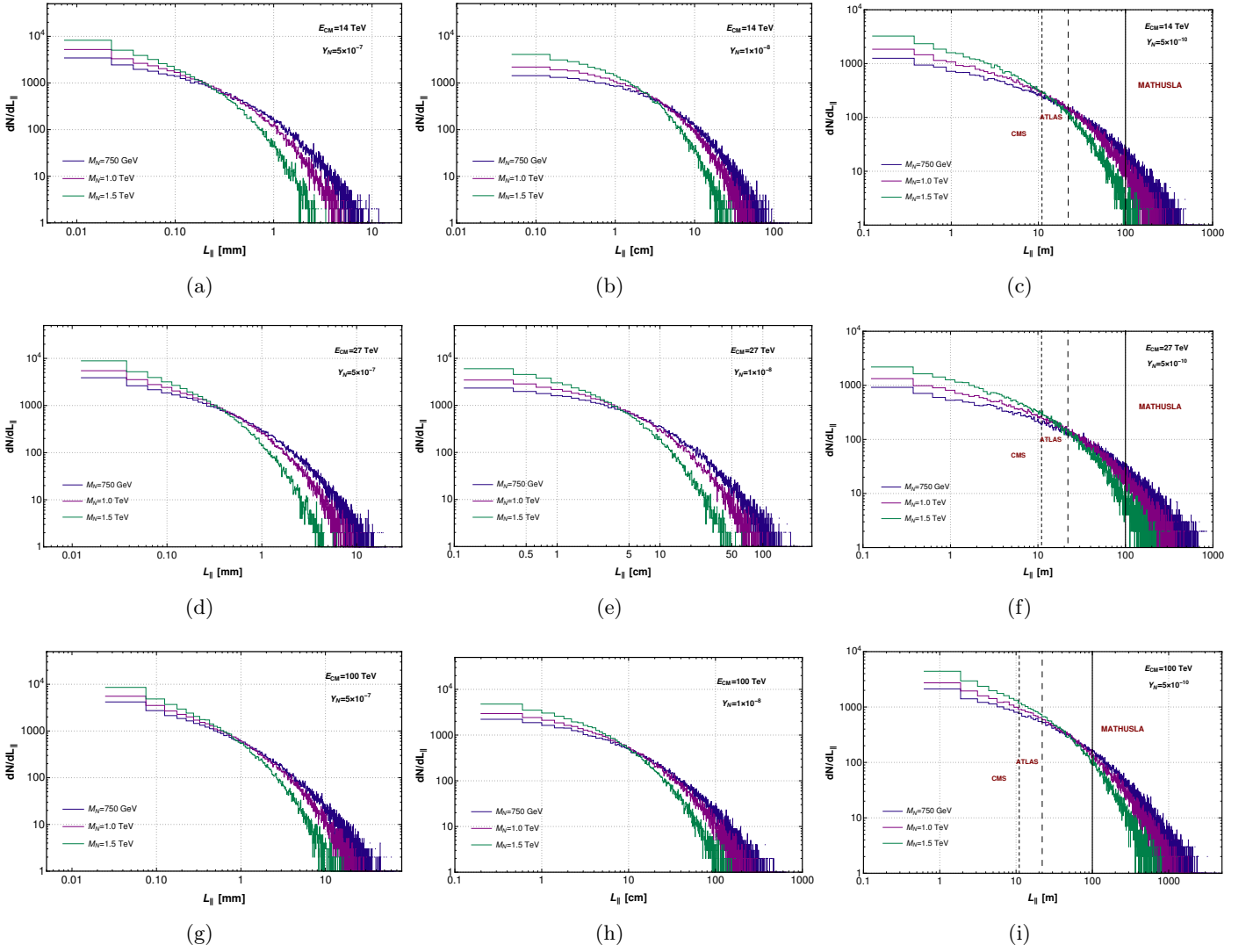


Figure 13. Displaced total longitudinal decay length (L_{\parallel}) distributions for the N^{\pm} , coming from the N^+N^- productions at the LHC with the centre of mass energies 14 TeV (a, b, c), 27 TeV (d, e, f) and 100 TeV (g, h, i) for the benchmark points. Yukawa couplings $Y_N = 5 \times 10^{-7}$, 1×10^{-8} , respectively are used for atmospheric (a, d, g) and solar (b, e, h) neutrino mass scales for $\mathcal{O}(100)$ GeV Type-III fermion mass, whereas the third column (c, f, i) depicts $Y_N = 5 \times 10^{-10}$, for higher reach. The dotted-dashed and dashed line indicates the upper limit of CMS and ATLAS, respectively. The solid black line denotes the lower limit of MATHUSLA.

goes from 14 TeV to 100 TeV, the transverse boost effect being negligible fails to enhance the corresponding decay lengths. Only points with $Y_N = 5 \times 10^{-10}$ in (c, f, i) can reach MATHUSLA region and rest of other Yukawa couplings correspond to less than a meter range.

The situation however changes drastically as we see the longitudinal displaced decay lengths due to larger boost effects as discussed before. In [Figure 13](#), we see the corresponding

total longitudinal displaced decay lengths incorporating both the recoils as explained before, for N^\pm , for the benchmark points at the LHC/FCC with centre of mass energies of 14, 27 and 100 TeV. Similar to the transverse case, here also the first column describes the $Y_N = 5 \times 10^{-7}$ (a, d, g), second column presents $Y_N = 1 \times 10^{-8}$ (b, e, h) and the third column corresponds to $Y_N = 5 \times 10^{-10}$ (c, f, i). The interesting point to note is that, now we have points greater than 1m for $Y_N = 10^{-8}$ and even outside MATHUSLA region, i.e. greater than 300 m for $Y_N = 5 \times 10^{-10}$. In Table 5, we present the number of events corresponding to transverse and longitudinal decay length inside MATHUSLA for the benchmark points conterminous with $Y_N = 5 \times 10^{-10}$ for the centre mass energies of 14, 27 and 100 TeV at an integrated luminosity of 3000 fb^{-1} , 1000 fb^{-1} and 300 fb^{-1} respectively. It is evident that the longitudinal mode has upper hand in terms of event numbers producing almost one order of magnitude more events. We will see that the situation is very unlikely in muon collider as total momentum is the same for each collision at a given energy. In the next subsection, we summarise the event numbers for various finalstates as well as the invariant mass reconstructions.

Number of events inside MATHUSLA with $Y_N = 5 \times 10^{-10}$.									
	$E_{CM} = 14 \text{ TeV}$			$E_{CM} = 27 \text{ TeV}$			$E_{CM} = 100 \text{ TeV}$		
	BP1	BP2	BP3	BP1	BP2	BP3	BP1	BP2	BP3
$100 \text{ m} \leq L_\perp \leq 125 \text{ m}$	354.8	28.8	0.3	778.2	108.5	3.6	3548.0	615.7	49.5
$100 \text{ m} \leq L_\parallel \leq 300 \text{ m}$	1081.0	95.4	1.0	3108.0	502.0	19.9	17200.0	3972.0	543.6

Table 5. The observed number of events in MATHUSLA detector in transverse and longitudinal direction for all benchmark points, with $Y_N = 5 \times 10^{-10}$ at the centre of mass energies of 14, 27 and 100 TeV at an integrated luminosity of 3000 fb^{-1} , 1000 fb^{-1} and 300 fb^{-1} , respectively. In transverse direction (L_\perp) the range of MATHUSLA is taken as 100 – 125 m, whereas in the longitudinal direction (L_\parallel) it is considered as 100 – 300 m.

5.3 Results

In this section, we focus on the decay channels $N^\pm \rightarrow h\ell^\pm$ and $N^0 \rightarrow h\nu$, where the Higgs boson further decays to $b\bar{b}$. We consider the possible finalstate with $2b$ -jets and more, which will later reconstruct the Higgs boson via their invariant mass peak. We also demand one or more charged leptons in the finalstate. The most dominant decay modes of $N^{\pm(0)} \rightarrow W^\pm\nu(\ell^\mp)$ for $Y_N \sim 10^{-7}$, only contributes to the finalstates with $2b$ -jets when the other one decays in $h\ell^\pm(\nu)$. In Table 6, we present the number of events for the finalstate topologies with $4b$ -jets and $2b$ -jets at the LHC, at the centre of mass energies of 14, 27 and 100 TeV with integrated luminosities of ($\mathcal{L}_{\text{int}}=$) 3000 fb^{-1} , 1000 fb^{-1} and 300 fb^{-1} , respectively, for all benchmark points and $Y_N = 5 \times 10^{-7}$. As the cross-section of $N^\pm N^0$ is almost twice as the pair production of N^\pm , $N^0 N^\pm$ is the dominant contributor as compared with the pair production of N^\pm for mono-leptonic finalstates. $N^+ N^-$ is the

Topologies	Modes	$E_{CM} = 14 \text{ TeV}$			$E_{CM} = 27 \text{ TeV}$			$E_{CM} = 100 \text{ TeV}$		
		BP1	BP2	BP3	BP1	BP2	BP3	BP1	BP2	BP3
$4b + 1\ell$	$N^0 N^\pm$	171.3	28.0	0.9	251.5	55.0	3.2	493.2	121.1	12.0
	$N^+ N^-$	32.6	6.0	0.2	61.1	11.7	0.8	124.8	42.4	4.6
	Total	203.9	34.0	1.1	312.6	66.7	4.0	618.0	163.5	16.6
$4b + \text{OSD}$	$N^0 N^\pm$	1.5	0.3	0.0	1.6	0.2	0.1	9.4	5.1	1.9
	$N^+ N^-$	58.5	10.8	0.2	111.6	17.7	1.2	206.4	54.8	6.1
	Total	60.0	11.1	0.2	113.2	17.9	1.3	215.8	59.9	8.0
$2b + 4j + 1\ell$	$N^0 N^\pm$	1728.0	321.9	17.9	2860.0	740.8	83.8	6492.0	2250.0	461.5
	$N^+ N^-$	1008.0	180.6	9.3	1671.0	417.5	42.0	4206.0	1392.0	253.3
	Total	2736.0	502.5	27.2	4531.0	1158.3	125.8	10698.0	3642.0	714.8
$2b + 4j + 2\ell$	$N^0 N^\pm$	654.0	116.2	4.6	1081.0	234.8	21.9	2003.0	632.7	113.0
	$N^+ N^-$	562.7	107.5	5.5	915.1	231.2	26.4	1983.0	757.6	136.3
	Total	1216.7	223.7	10.1	1996.1	466.0	48.3	3986.0	1390.3	249.3
$2b + 2j + 2\ell$	$N^0 N^\pm$	1058.0	191.4	7.9	1621.0	378.7	34.0	2999.0	977.2	159.3
	$N^+ N^-$	1046.0	205.8	12.3	1679.0	441.1	54.0	3428.0	1316.0	253.5
	Total	2104.0	397.2	20.2	3300.0	819.8	88.0	6427.0	2293.2	412.8
$2b + 2j + 3\ell$	$N^0 N^\pm$	262.0	45.8	2.2	381.8	89.8	7.8	791.5	222.5	34.1
	$N^+ N^-$	28.3	5.1	0.3	47.2	12.1	0.8	104.4	34.0	5.9
	Total	290.3	50.9	2.5	429.0	101.9	8.6	895.9	256.5	40.0

Table 6. Number of events for finalstate topologies containing at least two b -jets for the benchmark points with the centre of mass energies of 14 TeV, 27 TeV and 100 TeV at the LHC with integrated luminosities of $(\mathcal{L}_{\text{int}}=)$ 3000 fb^{-1} , 1000 fb^{-1} and 300 fb^{-1} respectively for $Y_N = 5 \times 10^{-7}$.

dominant contributor for the finalstates with more than one charged lepton. We see that the integrated luminosity can be one order of magnitude lower as we go from 14 TeV to 100 TeV collisions even for larger number of events.

The similar finalstate topologies have been studied for the benchmark points at the centre of mass energies of 14, 27 and 100 TeV with integrated luminosities of $(\mathcal{L}_{\text{int}}=)$ 3000 fb^{-1} , 1000 fb^{-1} and 300 fb^{-1} , respectively for $Y_N = 1 \times 10^{-8}$ in Table 7. Here, N^\pm dominantly decays to $N^0 \pi^\pm$ with $\mathcal{B}(N^\pm \rightarrow N^0 \pi^\pm) \sim 84\%$ for $M_N = 1 \text{ TeV}$, resulting a first recoil at around a few cm distance as discussed before. N^0 then follows the standard

Topologies	Modes	$E_{CM} = 14 \text{ TeV}$			$E_{CM} = 27 \text{ TeV}$			$E_{CM} = 100 \text{ TeV}$		
		BP1	BP2	BP3	BP1	BP2	BP3	BP1	BP2	BP3
$4b + 1\ell$	$N^0 N^\pm$	29.1	4.2	0.1	32.8	9.7	1.1	61.0	23.9	4.2
	$N^+ N^-$	18.0	3.2	0.2	33.3	6.1	0.8	76.7	22.0	4.4
	Total	47.1	7.4	0.3	66.1	15.8	1.9	137.7	45.9	8.6
$4b + \text{OSD}$	$N^0 N^\pm$	0.5	0.1	0.0	4.1	0.5	0.2	0.0	0.0	0.2
	$N^+ N^-$	1.6	0.5	0.0	4.0	0.8	0.1	7.2	3.0	0.2
	Total	2.1	0.6	0.0	8.1	1.3	0.3	7.2	3.0	0.4
$2b + 4j + 1\ell$	$N^0 N^\pm$	1522.0	285.8	12.8	2481.0	580.2	58.3	5266.0	1733.0	310.2
	$N^+ N^-$	722.9	133.3	6.3	1254.0	305.0	31.2	2899.0	963.4	178.4
	Total	2244.9	419.1	19.1	3735.0	885.2	89.5	8165.0	2696.4	488.6
$2b + 4j + 2\ell$	$N^0 N^\pm$	222.5	47.4	2.3	386.7	106.5	9.3	893.7	293.5	62.0
	$N^+ N^-$	126.2	27.2	1.4	205.8	61.6	7.0	538.0	210.6	40.5
	Total	348.7	74.6	3.7	592.5	168.1	16.3	1431.7	504.1	102.5
$2b + 2j + 2\ell$	$N^0 N^\pm$	634.9	119.6	5.8	952.7	234.7	21.6	1804.0	640.7	107.7
	$N^+ N^-$	313.6	61.2	3.2	480.2	129.8	13.5	1075.0	376.8	69.3
	Total	948.5	180.8	9.0	1432.9	364.5	35.1	2879.0	1017.5	177.0
$2b + 2j + 3\ell$	$N^0 N^\pm$	34.9	11.0	0.5	48.3	15.4	2.5	129.0	53.7	11.8
	$N^+ N^-$	37.9	5.4	0.4	52.7	12.3	1.9	106.6	46.6	9.5
	Total	72.8	16.4	0.9	101.0	27.7	4.4	235.6	100.3	21.3

Table 7. Number of events for finalstate topologies containing at least two b -jets for the benchmark points with the centre of mass energies of 14 TeV, 27 TeV and 100 TeV at the LHC with integrated luminosities of ($\mathcal{L}_{\text{int}} =$) 3000 fb^{-1} , 1000 fb^{-1} and 300 fb^{-1} respectively for $Y_N = 1 \times 10^{-8}$.

decay branching ratios to the SM modes. The presence of a charged pion instead of a charged lepton reduces the number of charged lepton in the finalstate. Along with that, it contributes to the hadronic jets, and lepton number can further shrink due to jet-lepton isolation criteria. Thus, the multi-lepton finalstates are a rarity as compared to the case of $Y_N = 5 \times 10^{-7}$. The main source of charged leptons in this case are from $N^0 \rightarrow W^\pm \ell^\mp$ and the further decays of the gauge bosons. This of course decrease the number of b -jets in the finalstate, which can be seen from the $4b + 1\ell$, $4b + 2\ell$ finalstates.

Thereafter we attempt to reconstruct the Higgs bosons from the bb invariant mass

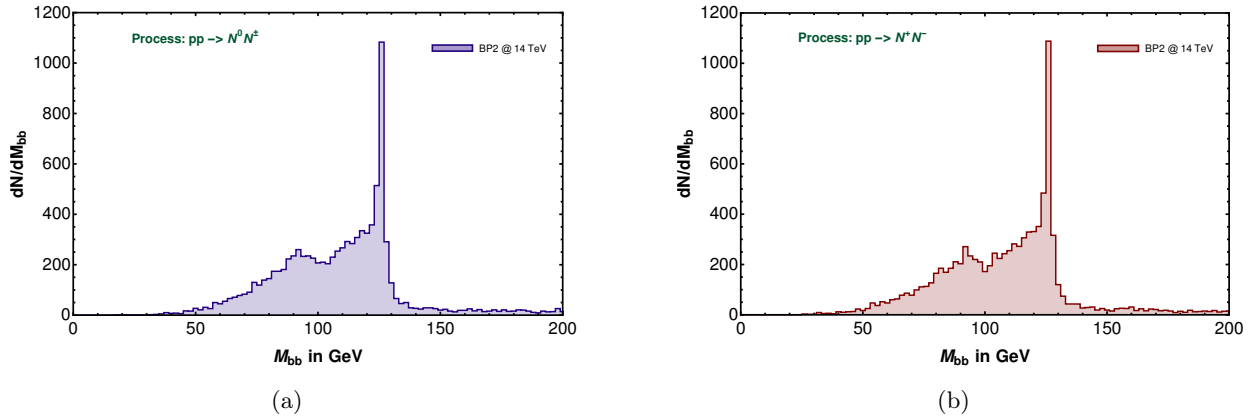


Figure 14. Di- b -jet invariant mass (M_{bb}) distributions for the process $pp \rightarrow N^0 N^\pm$ (a) and $pp \rightarrow N^+ N^-$ (b) at the LHC with $M_N = 1$ TeV (BP2), $Y_N = 1 \times 10^{-8}$ and center of mass energy of 14 TeV. The dominant peak around the SM Higgs mass (125.5 GeV) along with a small peak around the Z boson mass (91.1 GeV) are visible.

Topologies	Modes	$E_{CM} = 14$ TeV			$E_{CM} = 27$ TeV			$E_{CM} = 100$ TeV		
		BP1	BP2	BP3	BP1	BP2	BP3	BP1	BP2	BP3
$2b$ & $ M_{bb} - 125.5 \leq 10$	$N^0 N^\pm$	1705.0	324.8	15.0	2599.0	664.7	58.0	5855.0	1895.0	287.9
	$N^+ N^-$	802.7	144.0	6.7	1245.0	320.5	28.1	2927.0	979.5	138.0
	Total	2507.7	468.8	21.7	3844.0	985.2	86.1	8782.0	2874.5	425.9
$4b$ & $ M_{bb} - 125.5 \leq 10$	$N^0 N^\pm$	17.5	2.2	0.1	22.1	2.8	0.2	49.3	14.5	0.1
	$N^+ N^-$	8.8	0.7	0.0	19.1	1.8	0.0	21.6	4.0	0.1
	Total	26.3	2.9	0.1	41.2	4.6	0.2	70.9	18.5	0.2

Table 8. The number of events for single Higgs boson and di-Higgs boson mass peaks after the window cuts around the peak of the invariant mass distributions at the LHC/FCC at the centre of mass energies of 14 TeV, 27 TeV and 100 TeV at the integrated luminosity ($\mathcal{L}_{\text{int}} =$) 3000 fb^{-1} , 1000 fb^{-1} and 300 fb^{-1} , respectively for the benchmark points with $Y_N = 5 \times 10^{-7}$.

distribution coming from both $N^\pm \rightarrow h\ell$ and $N^0 \rightarrow h\nu$, as shown in Figure 14. We can observe the sharp peaks of Higgs boson around 125 GeV for both cases and a smaller peak around the Z boson mass, which comes from $N^\pm \rightarrow Z\ell^\pm$ and $N^0 \rightarrow Z\nu$ decays. The events around the Higgs mass certainly guarantees the finalstate with at least one Higgs boson and two Higgs bosons, which are described in Table 8. A demand of $|M_{bb} - 125.5| \leq 10$ GeV is made for single Higgs boson reconstruction. The numbers for the finalstates of $2b$ - and $4b$ -jets with the mass windows are shown in Table 8 at the centre of mass energies of 14 TeV, 27 TeV and 100 TeV at the integrated luminosity ($\mathcal{L}_{\text{int}} =$) 3000 fb^{-1} , 1000 fb^{-1} and 300 fb^{-1} for benchmark points with $Y_N = 5 \times 10^{-7}$. We see that though the number of events are quite healthy for single Higgs boson reconstruction, the same cannot be said for

two Higgs boson reconstructions coming from the two legs of Type-III fermions.

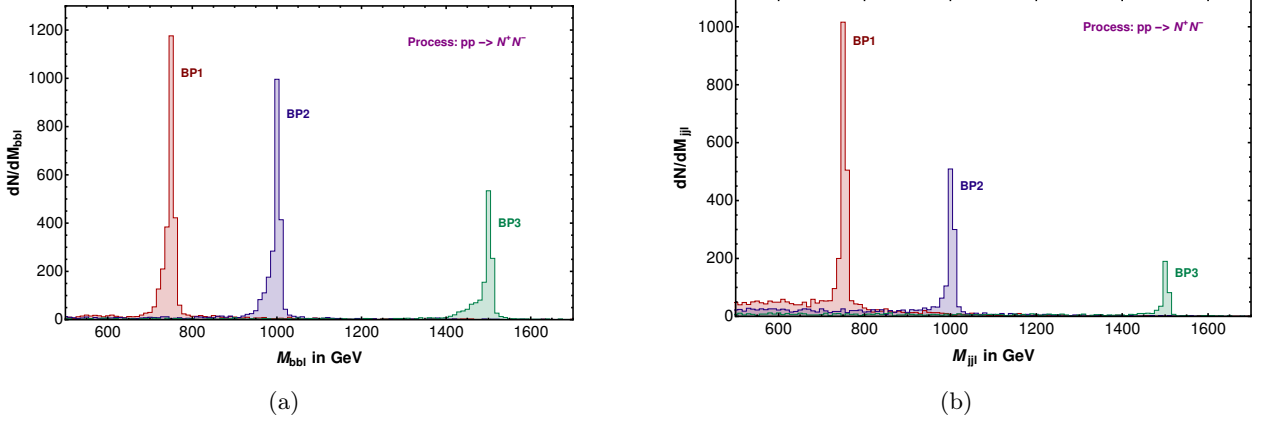


Figure 15. (a) Di-bjet-mono-lepton invariant mass ($M_{bb\ell}$) distribution for the process $pp \rightarrow N^+ N^-$ with $Y_N = 5 \times 10^{-7}$ (b) di-jet-mono-lepton ($M_{jj\ell}$) invariant mass distributions for the process $pp \rightarrow N^+ N^-$ with $Y_N = 1 \times 10^{-8}$ for the benchmark points at the LHC with centre of mass energy 14 TeV.

Benchmark Points	Topologies	Centre of mass energy		
		14 TeV	27 TeV	100 TeV
BP1	$2b + 1\ell$ & $ M_{bb\ell} - 750.0 \leq 10$	379.6	573.7	1223.0
BP2	$2b + 1\ell$ & $ M_{bb\ell} - 1000.0 \leq 10$	64.6	144.0	370.8
BP3	$2b + 1\ell$ & $ M_{bb\ell} - 1500.0 \leq 10$	2.8	11.4	50.0

Table 9. The number of events in $M_{bb\ell}$ distributions for $N^+ N^-$ after the window cuts around the mass peak at the LHC/FCC for the benchmark points at the centre of mass energies of 14 TeV, 27 TeV and 100 TeV at the integrated luminosities of ($\mathcal{L}_{\text{int}} =$) 3000 fb^{-1} , 1000 fb^{-1} and 300 fb^{-1} respectively with $Y_N = 5 \times 10^{-7}$.

Finally, we plot the invariant mass distributions of $bb\ell$ in Figure 15(a) in order to reconstruct the mass of Type-III fermion N^\pm . Here we ensure $|M_{bb} - 125.5| \leq 10$ GeV while reconstructing $M_{bb\ell}$. The three peaks visible at 750, 1000 and 1500 GeV are reconstructed for BP1, BP2 and BP3, respectively for $Y_N = 5 \times 10^{-7}$, where, $\mathcal{B}(N^\pm \rightarrow h\ell^\pm) \sim 25\%$. Similar to the previous case, here also we collect the events with a mass window of $|M_{bb\ell} - M_N| \leq 10$ GeV, to predict the number of events in Table 9. The table describes event

Benchmark Points	Topologies	Centre of mass energy		
		14 TeV	27 TeV	100 TeV
BP1	$2j + 1\ell$ & $ M_{jj\ell} - 750.0 \leq 10$	341.4	486.6	1087.0
BP2	$2j + 1\ell$ & $ M_{jj\ell} - 1000.0 \leq 10$	38.0	74.4	196.0
BP3	$2j + 1\ell$ & $ M_{jj\ell} - 1500.0 \leq 10$	0.9	3.0	13.7

Table 10. The number of events in $M_{jj\ell}$ distributions after the window cuts around the mass peak at the LHC/FCC for the benchmark points at the centre of mass energies of 14 TeV, 27 TeV and 100 TeV at the integrated luminosities of ($\mathcal{L}_{\text{int}}=$) 3000 fb^{-1} , 1000 fb^{-1} and 300 fb^{-1} respectively with $Y_N = 1 \times 10^{-8}$.

numbers for the benchmark points for the centre of mass energies of 14 TeV, 27 TeV and 100 TeV at the integrated luminosity ($\mathcal{L}_{\text{int}}=$) 3000 fb^{-1} , 1000 fb^{-1} and 300 fb^{-1} respectively with $Y_N = 5 \times 10^{-7}$. As we move from BP1 to BP3, keeping the centre of mass energy same we see event number drops as the cross-section decreases simultaneously. Certainly, the analysis predicts LHC/FCC with higher energy and luminosity will have much higher reach, which we discuss in [section 7](#).

In [Figure 15\(b\)](#) we present the invariant mass of di-jet-lepton coming from N^0 , which is produced from $N^\pm \rightarrow \pi^\pm N^0$ decay for lower Yukawa $Y_N = 10^{-8}$ for the benchmark points at the centre of mass energy of 14 TeV. The N^0 produced from such decays give rise to $W^\pm \ell^\mp$ dominantly and we reconstruct such W^\pm bosons from the di-jet invariant mass peak and select the events within $|M_{jj} - M_W| \leq 10 \text{ GeV}$ for further reconstruction of $M_{jj\ell}$. The corresponding events numbers are presented in [Table 10](#) for the centre of mass energies of 14 TeV, 27 TeV and 100 TeV at the integrated luminosities of ($\mathcal{L}_{\text{int}}=$) 3000 fb^{-1} , 1000 fb^{-1} and 300 fb^{-1} respectively. Due to large boost effect the two-jets coming from W^\pm decay combine as a single Fat-jet and we loose some events while reconstructing di-jet-lepton invariant mass distribution. The more we go for higher Type-III fermion mass the more prominent is such effect as the cross-sections still governs by on-shell productions.

Next, we indulge in measuring the transverse invariant mass distribution, where we have only one neutrino in the finalstate. While we produce $N^\pm N^0$ at the LHC, $N^\pm \rightarrow Z\ell$ and $N^0 \rightarrow h\nu$ decays give rise to finalstate with one neutrino, keeping other leg completely visible. The transverse invariant mass [65] of N^0 in such finalstate is constructed via the transverse energy and momenta of Higgs boson reconstituted from the di- b -jet and missing neutrino as

$$M_T^2 = m_h^2 + 2 \left(E_T^h \cancel{E}_T - \vec{p}_T^h \cdot \vec{\cancel{p}}_T \right), \quad (5.1)$$

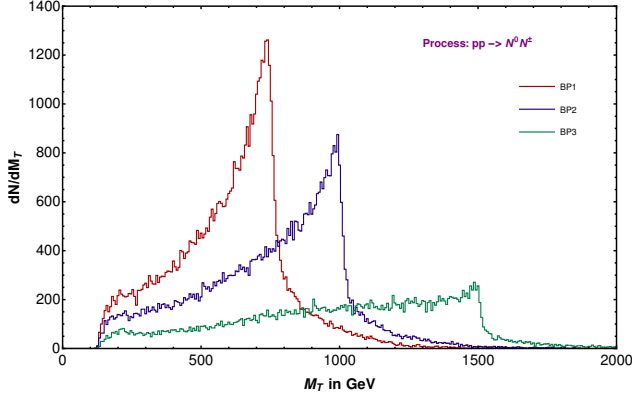


Figure 16. The transverse invariant mass (M_T) distribution for the process $pp \rightarrow N^0 N^\pm$, for the benchmark points at the LHC with $Y_N = 5 \times 10^{-7}$ and center of mass energy 14 TeV.

where E_T^h, p_T^h are the transverse energy and momenta, respectively of the Higgs boson reconstructed via di- b -jets. In Figure 16, we depict the transverse invariant mass of $bb\nu$ coming from N^0 , for $Y_N = 5 \times 10^{-7}$, where the other leg is tagged via complete visible mode such that, there is only one neutrino in the finalstate. In this case, missing p_T is equivalent to neutrino p_T . From Figure 16 we see the edge of the distributions depict the N^0 masses for the three benchmark points at the centre of mass energy of 14 TeV.

Benchmark Points	Topologies	Centre of mass energy		
		14 TeV	27 TeV	100 TeV
BP1	$2b \ \&$ $ M_T - 750.0 \leq 10$	18.6	26.1	49.3
BP2	$2b \ \&$ $ M_T - 1000.0 \leq 10$	2.5	4.7	11.8
BP3	$2b \ \&$ $ M_T - 1500.0 \leq 10$	0.1	0.2	1.1

Table 11. The number of events in M_T distributions after the window cuts around the mass peak at the LHC/FCC for the benchmark points at the centre of mass energies of 14 TeV, 27 TeV and 100 TeV at the integrated luminosities of ($\mathcal{L}_{\text{int}}=$) 3000 fb^{-1} , 1000 fb^{-1} and 300 fb^{-1} respectively with $Y_N = 5 \times 10^{-7}$.

The number of events correlated with the transverse invariant mass distribution, i.e. $|M_T - M_N| \leq 10 \text{ GeV}$ is presented in Table 11 for the benchmark points with the centre of mass energies of 14, 27 and 100 TeV at the integrated luminosities of ($\mathcal{L}_{\text{int}}=$) 3000 fb^{-1} , 1000 fb^{-1} and 300 fb^{-1} respectively with $Y_N = 5 \times 10^{-7}$. We ensure that the di- b -jet invariant

mass is peaking at the Higgs mass by selecting the events under $|M_{bb} - 125.5| \leq 10$ GeV

6 Simulation at the muon collider

Muon collider is proposed for the precision measurements as well as sensitive to processes involving lepton flavours. There is a recent buzz among the physicist where different BSM scenarios are explored [42–54]. The proposed optimistic reach of muon collider is around 90 ab^{-1} with centre of mass energy of 30 TeV [42]. Lack of initial state QCD radiation and known centre of mass energy for the collision makes it a superior machine over LHC. In this section, we investigate the displaced Higgs production by observing charged tracks coming from the decays of Type-III fermions. Unlike at LHC, in a muon collider, the centre of mass energy is equal to the parton level collision energy; thus the kinematical distributions will differ from that of LHC. Below we describe the kinematical distributions before presenting the results. We follow the same isolation criteria and minimum p_T cut for the jets and the leptons as described in section 4.

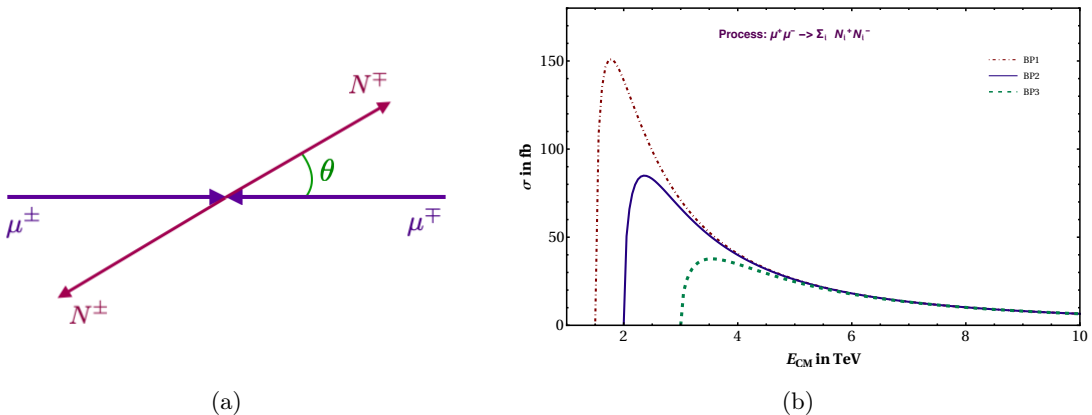


Figure 17. (a) The Feynman diagram and (b) the inclusive cross-sections (in fb) as a function of centre of mass energy (E_{CM}) for the benchmark points at muon collider for the process $\mu^+\mu^- \rightarrow \Sigma_i N_i^+ N_i^-$, where i ($= 1, 2, 3$) is the generation index. θ is the polar angle with the beam axis.

At the muon collider, N^\pm can be pair produced via Z boson and photon while production of $N^\pm N^0$ is not possible, unlike at the LHC/FCC, but pair production of N^0 is possible via N^\pm decay for relatively lower Yukawa couplings i.e. $Y_N \leq 10^{-8}$. Figure 17(a) presents the Feynman diagram of production of N^+N^- and θ represents the polar angle with the beam axis. Figure 17(b) present the cross-section for $\mu^+\mu^- \rightarrow N^+N^-$ with respect to centre of mass energy for the three benchmark points. It can be seen that the off-shell cross-sections drop very quickly, which implies very high energy is not efficient to probe these heavy neutrinos, unlike at the LHC. The cross-section can always find the on-shell resonant mode due to the parton distribution function at the LHC.

The cross-sections for the benchmark points at three different energies of muon colliders are presented in Table 12. We see that the cross-sections drop by an order for each as we

Benchmark points	E_{CM}		
	$\sigma_{\mu^+\mu^-\rightarrow\Sigma_i N_i^+ N_i^-}$ (in fb)		
	3.5 TeV	14 TeV	30 TeV
BP1	52.77	3.34	0.73
BP2	51.06	3.33	0.73
BP3	37.68	3.33	0.73

Table 12. Inclusive production cross-sections (in fb) of $\Sigma_i N_i^+ N_i^-$ for all benchmark points at muon collider for the centre of mass energies of 3.5 TeV, 14 TeV and 30 TeV, where i ($= 1, 2, 3$) is the generation index.

increase the centre of mass energy. Certainly, we need to achieve 30 ab^{-1} of integrated luminosity for the centre of mass energy of 30 TeV. In the following subsections, we study the kinematics of the hard scattering, i.e. of N^\pm . As opposed to LHC, here the system is in the centre of momentum frame keeping the three momenta constant along with the energy, and the only variable is the polar angle with the beam axis, i.e. θ .

6.1 Kinematical distributions

We begin by simulating the hard process, i.e. the kinematics of the N^\pm , which is summarised in Figure 18. The components of the three momentum of N^\pm , i.e. $p_x^{N^\pm}$, $p_y^{N^\pm}$, $p_z^{N^\pm}$ are shown in Figure 18(a), where it is evident that the events are populated at larger $p_z^{N^\pm}$ as compared to $p_x^{N^\pm}$, $p_y^{N^\pm}$. This doesn't come as surprise since the angular distribution of $\mu^+\mu^- \rightarrow N^+N^-$ in the centre of mass frame as given in Figure 18 (b), i.e. $\frac{d\sigma}{d\cos\theta} \sim (1 + \cos^2\theta)$ [66], thus the probability is more for $\cos\theta = \pm 1$, where $p_z^{N^\pm}$ is large. This can also be interpreted as follows: the longitudinal momentum $p_z^{N^\pm} = p^{N^\pm} \cos\theta$ and the transverse momentum $p_T^{N^\pm} = p^{N^\pm} \sin\theta$ are anti-correlated, which is apparent from Figure 18 (c). $p_z^{N^\pm}$ and $p_T^{N^\pm}$ peak at different angles, i.e. $\theta = 0, \pi$ for the former and $\theta = \pi/2, 3\pi/2$ for the latter. As the total momentum is conserved and finite, the distribution of $p_T^{N^\pm}$ forms a circular pattern with radius p , and $p_z^{N^\pm}$ project the gradient as $|\vec{p}|$ which can be seen from Figure 18(d).

However, if we plot the differential distributions with respect to $p_z^{N^\pm}$, it boils down to

$$\frac{d\sigma}{dp_z^{N^\pm}} = \frac{d\sigma}{d\cos\theta} \frac{d\cos\theta}{dp_z^{N^\pm}} = \frac{1}{p^{N^\pm}} \frac{d\sigma}{d\cos\theta} \simeq \frac{1}{p^{N^\pm}} (1 + \cos^2\theta). \quad (6.1)$$

Thus given a constant momentum for the N^\pm , i.e. $p^{N^\pm} = \text{constant} \neq 0$, $\frac{d\sigma}{dp_z^{N^\pm}}$ never diverges. On the contrary, the situation is quite different for transverse momentum distributions as

$$\frac{d\sigma}{dp_T^{N^\pm}} = \frac{d\sigma}{d\cos\theta} \frac{d\cos\theta}{dp_T^{N^\pm}} = \frac{1}{p^{N^\pm}} \frac{d\sigma}{d\cos\theta} \frac{d\cos\theta}{d\sin\theta} \simeq \frac{\tan\theta}{-p^{N^\pm}} (1 + \cos^2\theta). \quad (6.2)$$

$p_T^{N^\pm}$ diverges at $\theta = \pi/2, 3\pi/2$, which is evident from Figure 19. Thus unlike at the LHC, here at the muon collider, the transverse momentum dominates, and so transverse decay

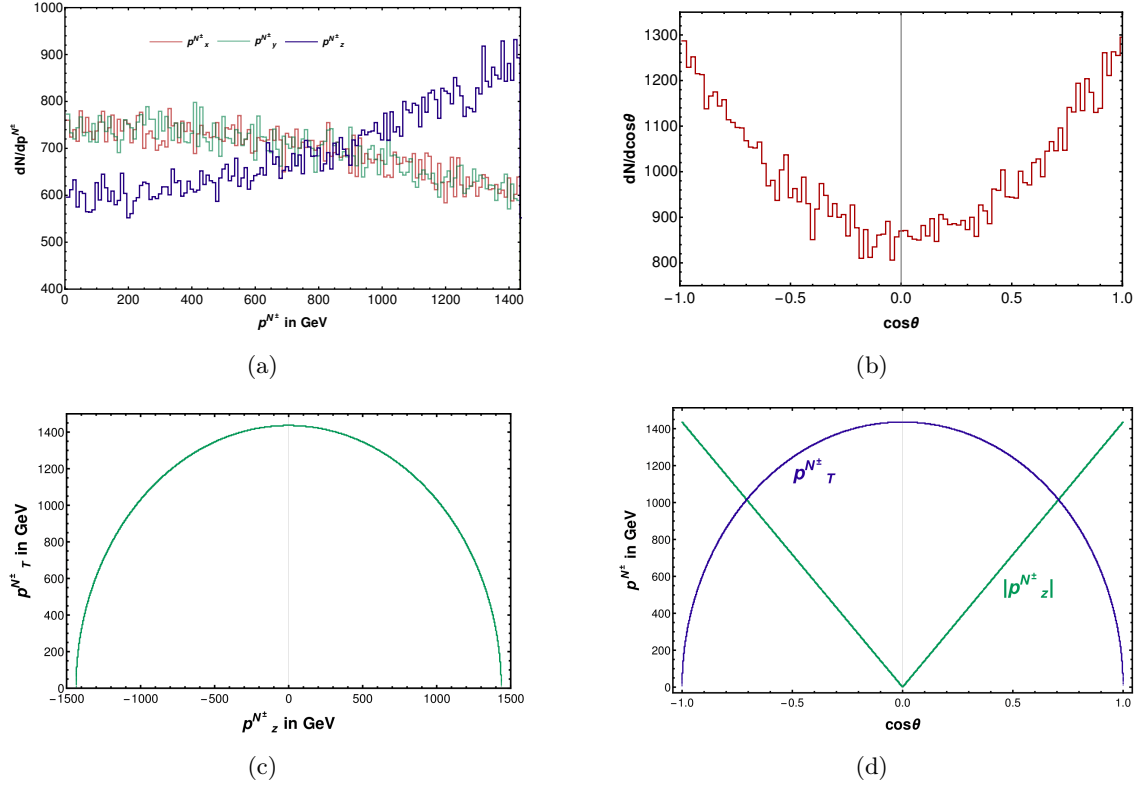


Figure 18. Various correlations of longitudinal ($p_z^{N^\pm}$) and transverse ($p_T^{N^\pm}$) momenta of N^\pm at muon collider with centre of mass energy of 3.5 TeV for BP2 for the process of $\mu^+\mu^- \rightarrow N^+N^-$. (a) Describes $p_x^{N^\pm}, p_y^{N^\pm}, p_z^{N^\pm}$, (b) presents the angular distribution of N^\pm . (c) describes correlation between $p_z^{N^\pm}$ and $p_T^{N^\pm}$ and (d) presents the correlation of $|p_z^{N^\pm}|$ and $p_T^{N^\pm}$ with respect to $\cos\theta$. For simplicity we remove the generation index i .

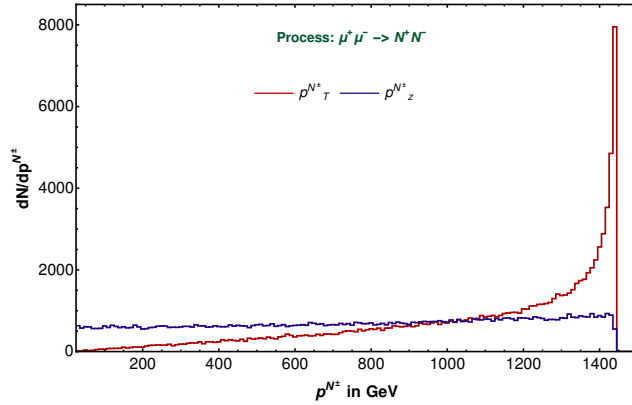


Figure 19. The transverse ($p_T^{N^\pm}$) and longitudinal ($p_z^{N^\pm}$) momenta distribution of the N^\pm at the muon collider with $M_N = 1$ TeV (BP2), $Y_N = 5 \times 10^{-7}$ and center of mass energy 3.5 TeV.

length can be expected to be slightly larger compared to the LHC/FCC. These effects are then transferred to the decayed leptons and jets from N^\pm . We should remember that this divergence also depends on the Lorentz structure of the matrix element, governed by the spin of the initial, final states and the propagator [66].

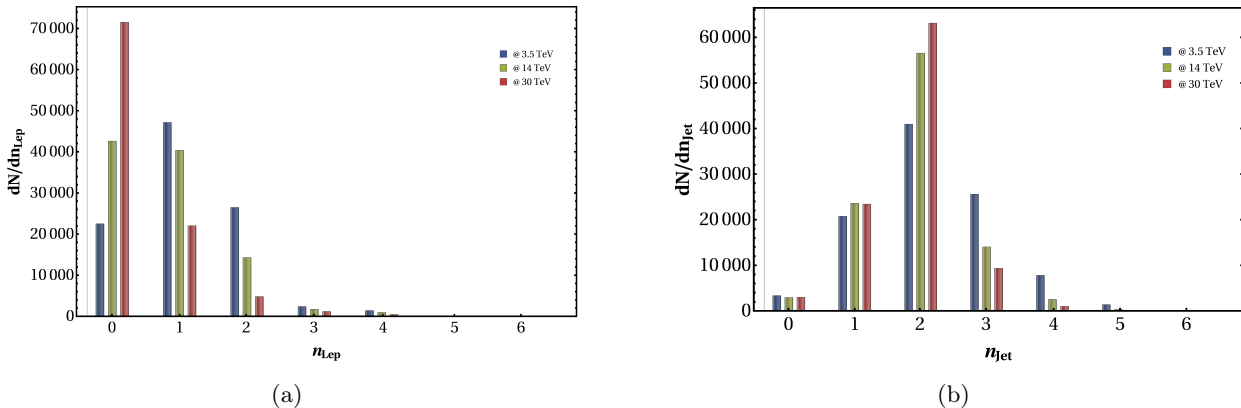


Figure 20. Multiplicity distributions (a) for the charged leptons (n_{Lep}) and (b) for the jets (n_{Jet}) at the centre of mass energies of 3.5 TeV, 14 TeV and 30 TeV for $M_N = 1$ TeV (BP2) and $Y_N = 5 \times 10^{-7}$ at the muon collider.

The kinematical features at the hard scattering level can decline when it comes to the final state decay products. Here we are focusing on N^\pm/N^0 giving rise to $h\ell^\pm/\nu$, and thus $2b$ -jets and one lepton (e, μ) or neutrino will be present in the final state. The jets and leptons are tagged via similar cuts as described in section 4. Figure 20 depicts the lepton and jet multiplicity distributions for BP2 with $Y_N = 5 \times 10^{-7}$ at three different energies. Figure 20(a) presents the lepton multiplicity distributions which remains similar to that at the LHC. However, in Figure 20(b) we have the jet multiplicity distributions, and the higher multiplicity is much lesser than at the LHC as muon collider is devoid of any initial state QCD radiations.

Figure 21 shows the lepton p_T distributions coming from $\mu^+\mu^- \rightarrow N^+N^-$ at the centre of mass energy of 3.5 TeV for the second benchmark point (BP2), where $M_N = 1$ TeV and $Y_N = 5 \times 10^{-7}$. Figure 21(a) presents the case, where the N^\pm is forced decayed to $e^\pm h$ and both the electrons have similar p_T distributions. Figure 21(b) depicts the case after the jet-lepton isolation where the yield of the second lepton is reduced. Finally, Figure 21(c) shows the distributions with the branching ratios of BP2. Here it can be noticed that the second lepton can either come from N^\pm or gauge bosons, while the first lepton mostly comes from N^\pm decays. The interesting point is the end point of the p_T distribution governed by the momentum conservation is limited to $\frac{E_{CM}}{2}$, unlike at the LHC/FCC.

Figure 22 depicts the p_T distributions of the first three p_T ordered jets for BP2 at the centre of mass energy of 3.5 TeV. The red curve representing the leading jet has two smooth peaks. The earlier one can be from the jets coming from the gauge bosons as well as from the Higgs boson decay. However, the higher peaks occur when two of these jets are merged due to the sufficient boost [57]. The second and third jets can come from gauge boson

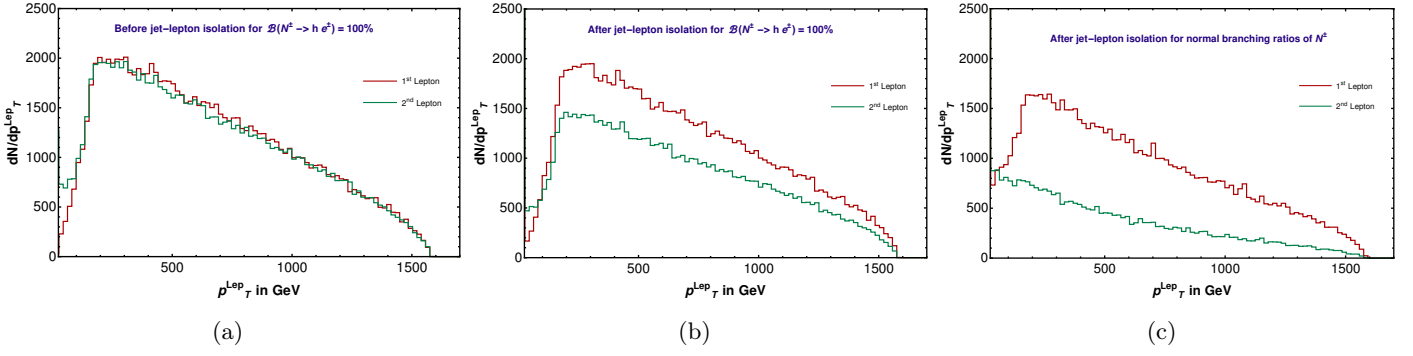


Figure 21. The transverse momentum (p_T) distributions of charged leptons (1^{st} and 2^{nd}) at the muon collider for $M_N = 1 \text{ TeV}$, $Y_N = 5 \times 10^{-7}$ and center of mass energy 3.5 TeV . (a) and (b) represent the distributions of two leptons for pre and post jet-lepton isolation, respectively for $\mathcal{B}(N^\pm \rightarrow h e^\pm) = 100\%$. (c) describes the scenario for the isolated leptons obeying the branching ratio of BP2.

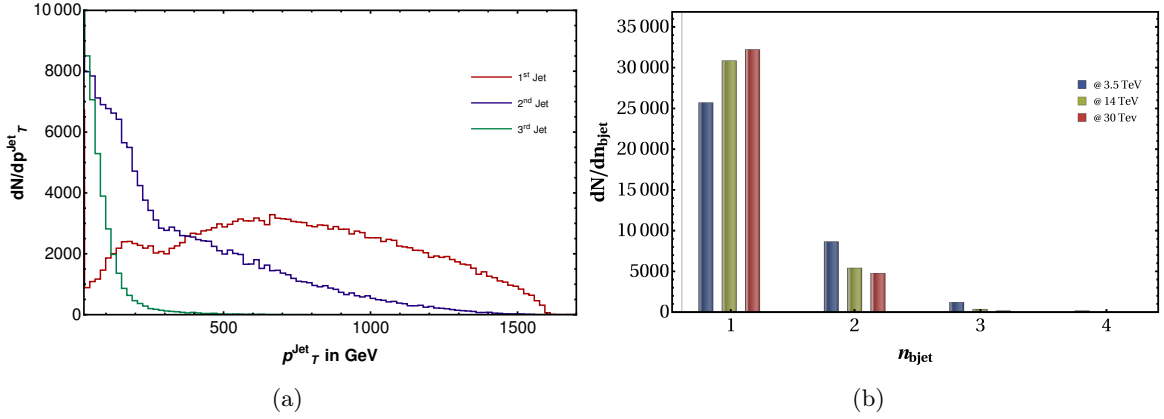


Figure 22. (a) The transverse momentum (p_T) distribution of the first three p_T ordered jets with the centre of mass energy of 3.5 TeV and (b) b -jet multiplicity distribution (n_{bjet}) at the muon collider for the centre of mass energies of 3.5 TeV , 14 TeV and 30 TeV , with $M_N = 1 \text{ TeV}$ (BP2), $Y_N = 5 \times 10^{-7}$.

decays. Along with these jets, there could be additional jets due to finalstate radiation (FSR) as evident from the jet multiplicity distributions in [Figure 20\(b\)](#). Contrary to the LHC/FCC, there cannot be any QCD radiation from the initial state in this case, so ISR effects are absent.

[Figure 22\(b\)](#) presents the b -jet multiplicity distributions. In spite of having four b -jets coming from the two Higgs bosons for BP2 at the centre of mass energy of 3.5 TeV , not all are tagged as b -jets due to the b -tagging efficiency. There can be b -jets coming from the Z boson decays as well. For the Higgs mass reconstructions we require at least two b -jets to be tagged which we discuss in the [subsection 6.4](#).

6.2 Boost effects at the muon collider

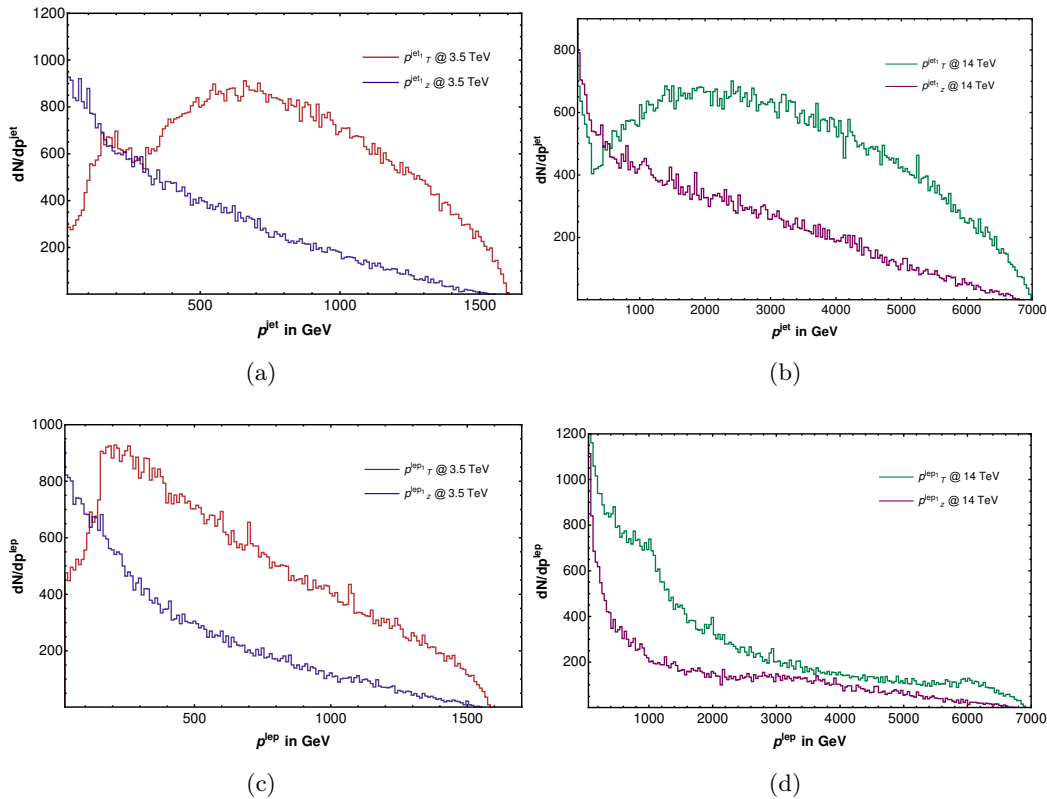


Figure 23. The transverse (p_T) and the longitudinal (p_z) momenta distributions at the muon collider for the process $\mu^+ \mu^- \rightarrow N^+ N^-$, with $M_N = 1$ TeV (BP2), $Y_N = 5 \times 10^{-7}$. (a) and (b) represent the distributions for leading jet with the centre of mass energies of 3.5 TeV and 14 TeV, respectively. (c) and (d) depict the similar distributions for isolated charged leptons.

Unlike at the LHC/FCC (as shown in [subsection 5.1](#)) in muon collider, the momentum conservation restricts the boost. Again, the angular distributions govern the behaviour of p_T and p_z , with the former diverging around $|\eta| \sim 0$. The resultant of these two, leads to p_T being more dominant over p_z for both jets and leptons, as described in [Figure 23](#). [Figure 23\(a\)](#) and [Figure 23\(b\)](#) show the p_T and p_z distributions of the leading jet for BP2 at the centre of mass energy of 3.5 and 14 TeV, respectively. We see the two-hump behaviour as before, which declines as we move from [Figure 23\(a\)](#) to [Figure 23\(b\)](#) due to larger boost which tends to create fat-jet like signatures [[57](#), [67–69](#)] at higher p_T values. Similar plots can be seen for the leptons in [Figure 23\(c\)](#) to [Figure 23\(d\)](#) where p_T remains dominant over p_z . Thus the boost effect on the decay length will be more on the transverse decay length than the longitudinal ones. This is contrary to what we observe at the LHC/FCC, where the partonic system is often boosted along z – direction governed by the parton distribution function, resulting in longer displaced decay length for the longitudinal ones as compared to the transverse one. This is an artifact that at the LHC/FCC the partonic momentum is

not fixed, unlike at the muon collider, where θ is the only parameter that varies.

6.3 Displaced decays at the muon collider

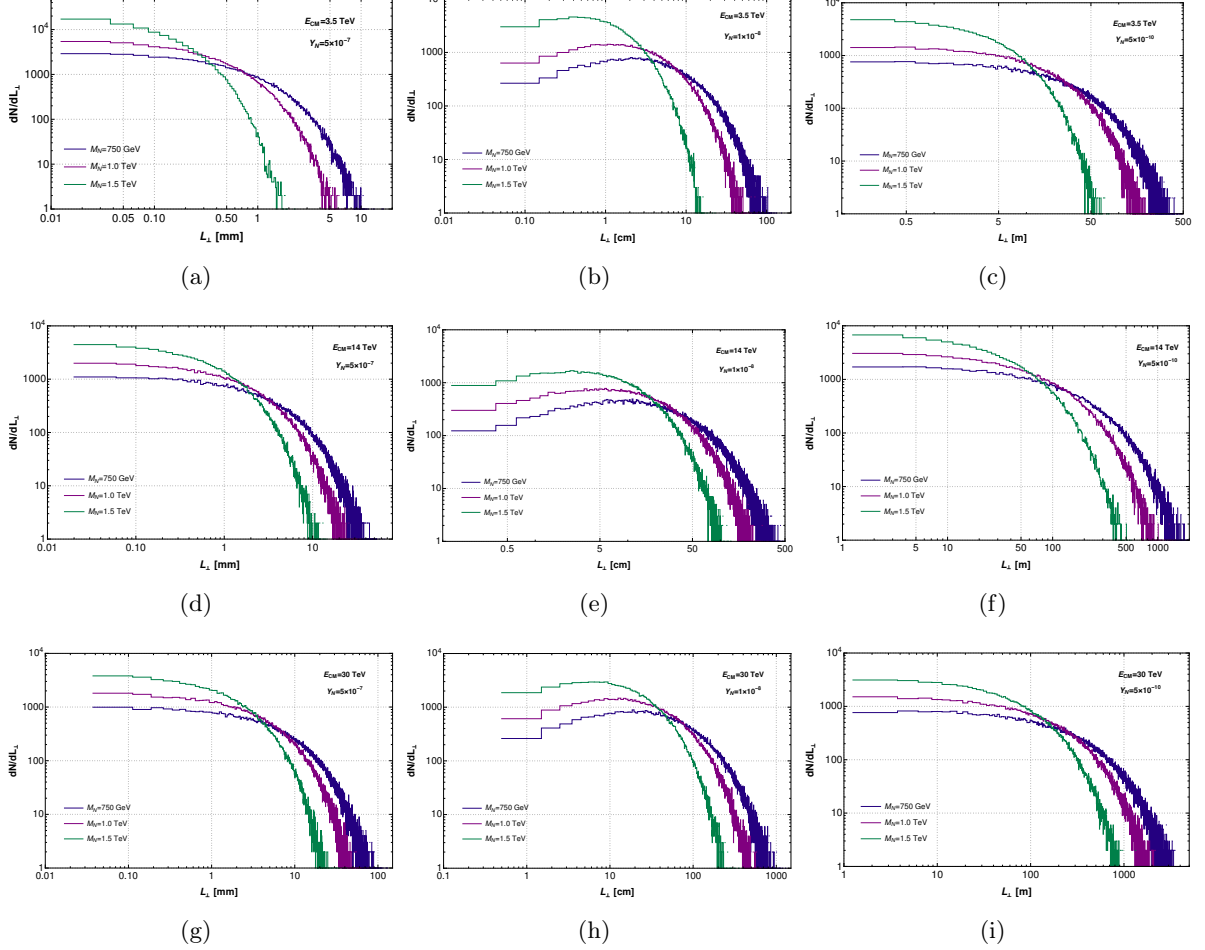


Figure 24. Displaced total transverse decay length (L_{\perp}) distributions for the $SU(2)_L$ triplet heavy fermions N^{\pm} , at the muon collider with the centre of mass energies of 3.5 TeV (a, b, c), 14 TeV (d, e, f) and 30 TeV (g, h, i) for the benchmark points. Yukawa coupling $Y_N = 5 \times 10^{-7}$, 1×10^{-8} , respectively are used for atmospheric (a, d, g) and solar (b, e, h) neutrino mass scales for $\mathcal{O}(100)$ GeV Type-III fermion mass, whereas the third column (c, f, i) depicts $Y_N = 5 \times 10^{-10}$ for a higher reach.

Displaced decays can also be observed at muon collider by observing charged tracks from N^{\pm} as they fly a certain distance before its decay. Figure 24 describes the transverse decay length distribution for the charged $SU(2)_L$ triplet heavy fermions N^{\pm} coming from $\mu^+\mu^- \rightarrow N^+N^-$ for the centre of mass energies of 3.5, 14 and 30 TeV for benchmark points. Column wise they describe the cases for three different Yukawa couplings 5×10^{-7} , 1×10^{-8} , 5×10^{-10} . $Y_N = 5 \times 10^{-7}$ is used in the first column for the atmospheric neutrino mass scale for $\mathcal{O}(100)$ GeV Type-III fermion mass. The maximum decay length is around 2 mm for $M_N = 1.5$

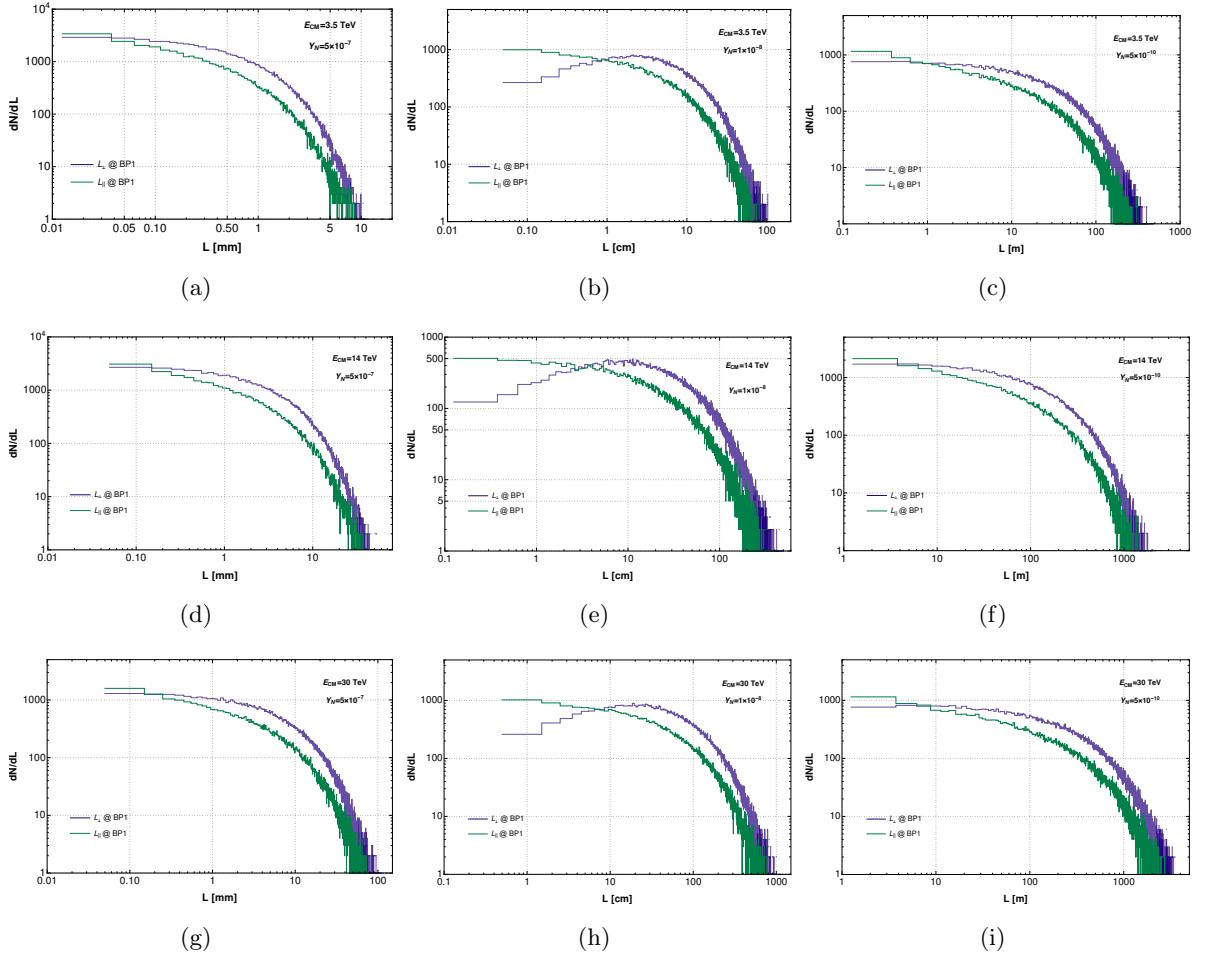


Figure 25. Displaced total transverse (L_{\perp}) and longitudinal (L_{\parallel}) decay length distributions for the $SU(2)_L$ triplet heavy fermions N^{\pm} , at the muon collider with the centre of mass energies of 3.5 TeV (a, b, c), 14 TeV (d, e, f) and 30 TeV (g, h, i) for BP1. Yukawa coupling $Y_N = 5 \times 10^{-7}$, 1×10^{-8} , respectively are used for atmospheric (a, d, g) and solar (b, e, h) neutrino mass scales for $\mathcal{O}(100)$ GeV Type-III fermion mass, whereas the third column (c, f, i) depicts $Y_N = 5 \times 10^{-10}$ for a higher reach.

TeV (green curve) at the centre of mass energy 3.5 TeV, but the boost effect enhances this to 10 mm and 20 mm at the centre of mass energies of 14 and 30 TeV, respectively.

While $Y_N = 1 \times 10^{-8}$ is used in the second column for the corresponding solar neutrino mass scale. In this case $N^{\pm} \rightarrow N^0 \pi^{\pm}$ is the dominant mode as we expect two decay recoils as discussed before and the total displaced decays are shown in Figure 24. The first one is for the $N^{\pm} \rightarrow N^0 \pi^{\pm}$, which is order of cm and the next one comes from N^0 decays which stays in the order of meter. It is evident that only for $Y_N = 5 \times 10^{-10}$ (third column), the total transverse decay length falls in the range of ~ 100 m for all three energies, while for the rest, we observe the signatures within 10 m range.

Due to enhanced transverse boost contrary to LHC as mentioned before, the total

	Number of events with $Y_N = 5 \times 10^{-10}$.								
	$E_{CM} = 3.5 \text{ TeV}$			$E_{CM} = 14 \text{ TeV}$			$E_{CM} = 30 \text{ TeV}$		
	BP1	BP2	BP3	BP1	BP2	BP3	BP1	BP2	BP3
$1 \text{ mm} \leq L_{\perp} \leq 10 \text{ m}$	1264.0	2090.0	2721.0	120.9	217.3	414.0	28.3	56.7	116.3
$10 \text{ m} < L_{\perp} \leq 100 \text{ m}$	3219.0	2648.0	669.4	658.9	973.7	1167.0	208.9	347.1	594.4
$1 \text{ mm} \leq L_{\parallel} \leq 10 \text{ m}$	835.3	1263.0	1482.0	113.4	172.1	294.0	32.2	54.7	106.9
$10 \text{ m} \leq L_{\parallel} \leq 100 \text{ m}$	1482.0	1111.0	186.2	377.3	491.3	531.6	140.5	216.7	298.1

Table 13. The number of events within the range 1 mm - 10 m and 10 m - 100 m in the transverse (L_{\perp}) and longitudinal (L_{\parallel}) direction for the benchmark points at the centre of mass energies of 3.5, 14 and 30 TeV with the integrated luminosities of ($\mathcal{L}_{\text{int}} =$) 1000 fb $^{-1}$, 10000 fb $^{-1}$ and 30000 fb $^{-1}$, respectively for $Y_N = 5 \times 10^{-10}$.

transverse displaced decay lengths are relatively inflated. In [Figure 25](#), we describe the longitudinal (in green) and transverse (in purple) displaced decay lengths for BP1 for the centre of mass energies of 3.5, 14 and 30 TeV at the muon collider. One can see the enhancement of the event numbers for the transverse ones, especially for $Y_N = 5 \times 10^{-10}$. For $Y_N = 10^{-8}, 5 \times 10^{-10}$ we have two recoils as described before and the total decay lengths are presented including the boost effects.

In [Table 13](#), we present the number of events for the longitudinal and transverse decay lengths for the benchmark points for the centre of mass energies of 3.5, 14 and 30 TeV at the integrated luminosity ($\mathcal{L}_{\text{int}} =$) 1000 fb $^{-1}$, 10000 fb $^{-1}$ and 30000 fb $^{-1}$, respectively with $Y_N = 5 \times 10^{-10}$. We separate two different regions, 1mm-10 m and 10-100 m, for those event numbers. For other Yukawa couplings chosen earlier, the events lie within the 10 m range. One very interesting feature to observe is that due to larger transverse boost the event number for the transverse decay length are more unlike at the LHC/FCC ([Table 5](#)).

6.4 Results

In this section, we describe the event numbers for the finalstates coming from the N^{\pm} decay and at least one Higgs bosons which is tagged via b -jets. Thus in [Table 14](#) (columns 3, 4, 5) we describe the finalstates with two and four b -jets for the benchmark points at the centre of mass energies 3.5 TeV, 14 TeV and 30 TeV at the muon collider with integrated luminosity ($\mathcal{L}_{\text{int}} =$) 1000 fb $^{-1}$, 10000 fb $^{-1}$, 30000 fb $^{-1}$, respectively for $Y_N = 5 \times 10^{-7}$. The b -tagging efficiency is taken to be maximum of 85% and dynamically set while simulating the events via secondary vertex reconstruction as explained earlier [[61](#), [62](#)]. The number of $4b$ -jets events are one order of magnitude less than that of $2b$ -jets events, where they are ideally coming via $N^{\pm} \rightarrow h\ell^{\pm}$, from both the legs. We see that the number of events for various finalstates reduce from 3.5 TeV to 30 TeV as we go more and more off-shell for all the benchmark points. All the finalstates described here are displaced ones and the event number ≥ 3 can be probed at 95% confidence level for the background-less signals [[70](#), [71](#)].

Center of mass energy	Topologies	$Y_N = 5 \times 10^{-7}$			$Y_N = 1 \times 10^{-8}$		
		BP1	BP2	BP3	BP1	BP2	BP3
3.5 TeV	$4b + 1\ell$	23.2	25.5	12.4	14.8	18.2	10.6
	$4b + \text{OSD}$	52.2	40.9	23.7	0.5	1.0	1.8
	$2b + 4j + 1\ell$	668.6	605.1	350.0	347.3	298.1	160.2
	$2b + 4j + 2\ell$	244.3	236.4	124.7	43.5	33.1	21.6
	$2b + 2j + 2\ell$	2028.0	2055.0	1420.0	450.7	446.7	320.1
	$2b + 2j + 3\ell$	52.2	48.5	27.9	41.6	47.9	37.6
14 TeV	$4b + 1\ell$	0.3	1.3	1.7	0.9	0.3	1.6
	$4b + \text{OSD}$	0.3	2.7	1.0	0.0	0.0	0.0
	$2b + 4j + 1\ell$	40.4	72.2	126.9	21.0	27.9	49.4
	$2b + 4j + 2\ell$	9.7	17.7	17.4	1.6	2.2	3.1
	$2b + 2j + 2\ell$	240.9	459.3	965.4	46.4	62.1	102.8
	$2b + 2j + 3\ell$	5.3	7.3	9.0	3.1	6.3	9.7
30 TeV	$4b + 1\ell$	0.0	0.2	0.0	0.0	0.2	0.4
	$4b + \text{OSD}$	0.0	0.2	0.4	0.0	0.0	0.0
	$2b + 4j + 1\ell$	4.8	10.7	24.5	1.6	2.9	5.8
	$2b + 4j + 2\ell$	0.9	1.3	3.5	0.0	0.0	1.2
	$2b + 2j + 2\ell$	21.4	51.1	153.0	11.9	16.2	19.6
	$2b + 2j + 3\ell$	0.4	2.0	2.4	0.0	0.6	3.1

Table 14. Number of events for finalstate topologies containing at least two b -jets for the benchmark points with the centre of mass energies of 3.5 TeV, 14 TeV and 30 TeV at the muon collider with integrated luminosities of ($\mathcal{L}_{\text{int}} =$) 1000 fb^{-1} , 10000 fb^{-1} , 30000 fb^{-1} , respectively with $Y_N = 5 \times 10^{-7}$ (columns 3, 4, 5) and with $Y_N = 1 \times 10^{-8}$ (columns 6, 7, 8).

Similarly, we present the event numbers for $Y_N = 10^{-8}$ in Table 14 (columns 6, 7, 8) for the above mentioned finalstates for the benchmark points with the centre of mass energies of 3.5 TeV, 14 TeV and 30 TeV at an integrated luminosities of ($\mathcal{L}_{\text{int}} =$) 1000 fb^{-1} , 10000 fb^{-1} , 30000 fb^{-1} , respectively. The multi-lepton finalstates suffer compared to the case of $Y_N = 10^{-7}$ due to lost charged lepton by the new decay mode of $N^\pm \rightarrow N^0 \pi^\pm$, which is very similar to that of the LHC results in Table 7.

Subsequently, we focus on the di- b -jet invariant mass reconstruction as shown in Figure 26 for BP2. We can see the two peaks coming from the Higgs and Z bosons distinctively. We impose the constraint of $|M_{bb} - 125.5| \leq 10 \text{ GeV}$, essential to reconstruct one Higgs boson mass peak. Following this approach, we tag at least one Higgs boson for the finalstate of $2b$ and two Higgs bosons for $4b$, which are listed in Table 15 for the centre of mass energies of 3.5 TeV, 14 TeV and 30 TeV at the integrated luminosity ($\mathcal{L}_{\text{int}} =$) 1000 fb^{-1} , 10000 fb^{-1}

and 30000 fb^{-1} , respectively for all benchmark points with $Y_N = 5 \times 10^{-5}$. From the event numbers we realise that only one Higgs boson reconstruction is feasible.

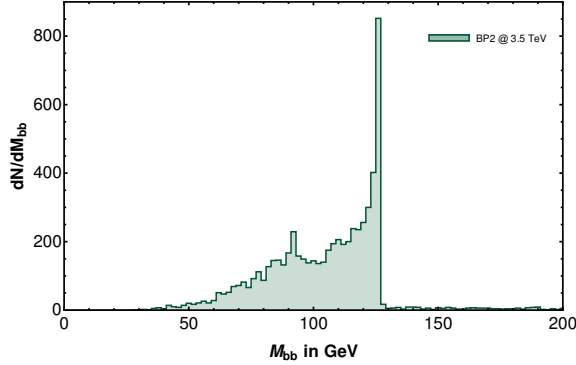


Figure 26. Di- b -jet (M_{bb}) invariant mass distributions for BP2 ($M_N = 1 \text{ TeV}$) at the muon collider with $Y_N = 5 \times 10^{-7}$ and centre of mass energy 3.5 TeV. The dominant peak around the SM Higgs boson mass (125.5 GeV) along with a small peak around the Z boson mass (91.1 GeV) are visible.

Topologies	$E_{CM} = 3.5 \text{ TeV}$			$E_{CM} = 14 \text{ TeV}$			$E_{CM} = 30 \text{ TeV}$		
	BP1	BP2	BP3	BP1	BP2	BP3	BP1	BP2	BP3
$2b \ \& \ M_{bb} - 125.5 \leq 10$	1128.0	1092.0	802.9	156.0	143.0	170.6	31.9	36.5	49.8
$4b \ \& \ M_{bb} - 125.5 \leq 10$	9.5	5.1	1.5	0.0	0.7	0.0	0.0	0.0	0.2

Table 15. Number of events for single Higgs boson and di-Higgs boson mass peaks after the window cuts around the peak of the invariant mass distributions for the benchmark points at the muon collider with the centre of mass energies of 3.5 TeV, 14 TeV and 30 TeV at the integrated luminosities of ($\mathcal{L}_{\text{int}} =$) 1000 fb^{-1} , 10000 fb^{-1} and 30000 fb^{-1} , respectively with $Y_N = 5 \times 10^{-7}$.

In [Figure 27\(a\)](#), we plot the $bb\ell$ invariant mass to reconstruct the N^\pm mass for the benchmark points. We can clearly see the three peaks for the three benchmark points. The corresponding number of events are projected in [Table 16](#) for the centre of mass energies of 3.5 TeV, 14 TeV and 30 TeV at the integrated luminosity ($\mathcal{L}_{\text{int}} =$) 1000 fb^{-1} , 10000 fb^{-1} and 30000 fb^{-1} , respectively with $Y_N = 5 \times 10^{-7}$. Thus the visible mode leading to $bb\ell$ can successfully reconstruct the Type-III fermion masses.

In [Figure 27\(b\)](#), we reconstruct the N^0 invariant mass for the case of $Y_N = 1 \times 10^{-8}$, where $N^\pm \rightarrow N^0 \pi^\pm$ is the dominant decay mode. The $N^0 \rightarrow W^\pm \ell^\mp$ is first reconstructed via the di-jet invariant mass peak around W^\pm mass by demanding $|M_{jj} - M_W| \leq 10 \text{ GeV}$. Later events are collected around that mass window to constitute $M_{jj\ell}$. It is evident from [Figure 27\(b\)](#) that $M_{jj\ell}$ peaks around M_N for the benchmark points at the centre of mass energy of 14 TeV. The corresponding event numbers are presented in [Table 17](#) for the benchmark points with the centre of mass energies of 3.5 TeV, 14 TeV and 30 TeV at the

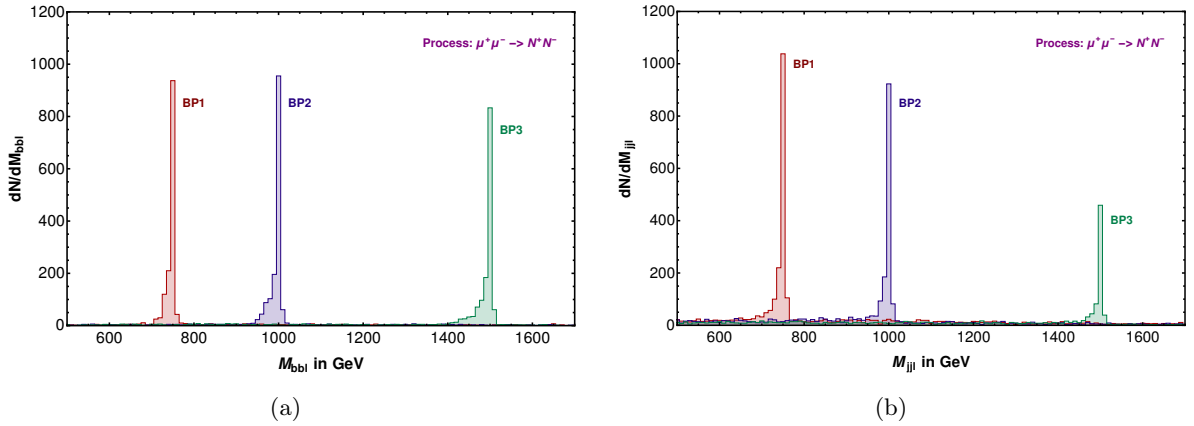


Figure 27. (a) Di-bjet-mono-lepton ($M_{bb\ell}$) invariant mass distribution with $Y_N = 5 \times 10^{-7}$, (b) di-jet-mono-lepton ($M_{jj\ell}$) invariant mass distributions with $Y_N = 1 \times 10^{-8}$ for the benchmark points at the muon collider with the centre of mass energy 3.5 TeV.

Benchmark points	Topologies	Centre of mass energy		
		3.5 TeV	14 TeV	30 TeV
BP1	$2b + 1\ell$ & $ M_{bb\ell} - 750.0 \leq 10$	548.3	31.7	2.6
BP2	$2b + 1\ell$ & $ M_{bb\ell} - 1000.0 \leq 10$	535.2	50.1	7.6
BP3	$2b + 1\ell$ & $ M_{bb\ell} - 1500.0 \leq 10$	351.5	61.1	14.2

Table 16. The number of events in $M_{bb\ell}$ distribution after the window cut around the mass peak for the benchmark points at the muon collider with the centre of mass energies of 3.5 TeV, 14 TeV and 30 TeV at the integrated luminosities of ($\mathcal{L}_{\text{int}}=$) 1000 fb $^{-1}$, 10000 fb $^{-1}$ and 30000 fb $^{-1}$, respectively with $Y_N = 5 \times 10^{-7}$.

integrated luminosities of ($\mathcal{L}_{\text{int}}=$) 1000 fb $^{-1}$, 10000 fb $^{-1}$ and 30000 fb $^{-1}$, respectively. We see similar effects of boost reducing the jet multiplicity for BP3 (see Table 10) and thus reducing the number of events for $M_{jj\ell}$. For higher energies of 14 and 30 TeV such effects are negligible as the off-shell cross-section remain very low.

7 Reach plots in Yukawa versus mass plane

In this section, we plot the regions in Yukawa versus mass plane that can be probed at the LHC/FCC and at the muon collider. The regions are obtained from the zero background analysis with a confidence level of 95% at a given luminosity [70, 71]. Figure 28 presents the regions in a plane of Type-III Yukawa coupling versus mass at the LHC with 14 TeV

Benchmark points	Topologies	Centre of mass energy		
		3.5 TeV	14 TeV	30 TeV
BP1	$2j + 1\ell$ & $ M_{jj\ell} - 750.0 \leq 10$	565.5	45.8	4.9
BP2	$2j + 1\ell$ & $ M_{jj\ell} - 1000.0 \leq 10$	481.7	42.3	7.6
BP3	$2j + 1\ell$ & $ M_{jj\ell} - 1500.0 \leq 10$	176.6	56.3	11.9

Table 17. The number of events in $M_{jj\ell}$ distribution after the window cut around the mass peak for the benchmark points at the muon collider with the centre of mass energies of 3.5 TeV, 14 TeV and 30 TeV at the integrated luminosities of ($\mathcal{L}_{\text{int}} =$) 1000 fb^{-1} , 10000 fb^{-1} and 30000 fb^{-1} , respectively with $Y_N = 1 \times 10^{-8}$.

and 100 TeV centre of mass energies that can be probed at an integrated luminosities of 3000 and 300 fb^{-1} , respectively. Bounds obtained here are solely from the displaced decay signatures and the LHC bounds from the prompt leptonic finalstates are not shown here [27–29].

In Figure 28(a), we see the bounds obtained from the transverse decay lengths at the CMS and ATLAS (in light green) and MATHUSLA (in brown) at the centre of mass energy of 14 TeV with an integrated luminosity of 3000 fb^{-1} . The corresponding longitudinal decay length bounds are presented in Figure 28(b). The maximum Type-III fermion mass of 2.4 TeV, 2.7 TeV can be probed via the transverse and the longitudinal displaced decay length at the LHC with centre of mass energy of 14 TeV with an integrated luminosity of 3000 fb^{-1} , respectively. The bounds at 100 TeV centre of mass energy are 3.8 TeV and 4.3 TeV, respectively for the transverse and the longitudinal decay lengths at an integrated luminosity of 300 fb^{-1} . At larger luminosity of 3000 fb^{-1} we can probe even higher mass range around 5.8 TeV. Though it is very small, we observe slight enhancement on the mass bounds in the longitudinal mode as compared to the transverse one. One also expects 15% enhancement in the reach considering the QCD corrections [72]. Yukawa couplings in the range of $5 \times 10^{-11} - 10^{-6}$ can be probed if we consider the inclusive measurements of LHC/FCC and MATHUSLA. The transverse and longitudinal reaches at the MATHUSLA are quite low as compared to CMS and ATLAS. Considering both the transverse and the longitudinal decay lengths, we see that Yukawa coupling $> 10^{-8}$ is out of the reach of MATHUSLA, however can be addressed at CMS and ATLAS.

In Figure 29, we depict the region plots at the muon collider for the centre of mass energies of 14 TeV and 30 TeV. In Figure 29(a) and (b), we present the regions that can be probed with transverse and longitudinal decay lengths of 1 mm to 10 m at the centre of mass energies of 14 and 30 TeV with integrated luminosities of 10000 and 30000 fb^{-1} , respectively. From Figure 29 (a) we see that the transverse decay length probes for $Y_N =$

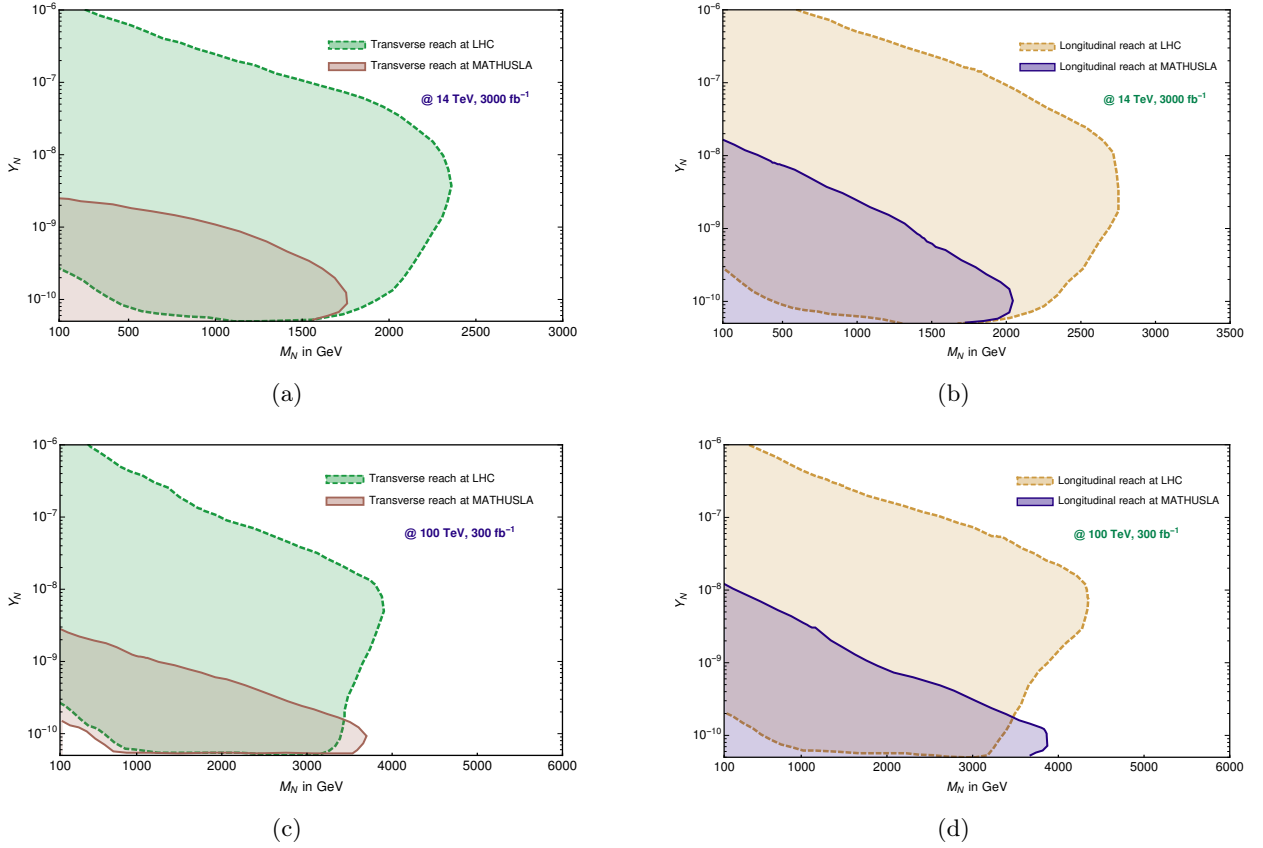


Figure 28. Limits obtained via the inclusive measurements from $N^0 N^\pm$, $N^+ N^-$ productions for the Yukawa coupling versus Type-III fermion mass for the transverse (a, c) and the longitudinal (b, d) decay lengths for the finalstates containing at least $2b$ -jets with 14 (a, b), 100 (c, d) TeV centre of mass energies at the LHC/FCC with integrated luminosities of 3000 and 300 fb^{-1} respectively.

10^{-7} , and mass ranges up to 4.2, 6.1 TeV for the centre of mass energies of 14, 30 TeV at the integrated luminosities of 10000 and 30000 fb^{-1} , respectively. The corresponding bounds from longitudinal decays can be estimated from [Figure 29](#) (b) as 3.5 and 5.4 TeV, respectively for the centre of mass energies of 14 and 30 TeV. Due to the momentum conservation the maximum mass ranges that can be probed are restricted to 7 and 15 TeV respectively for the centre of mass energies of 14 and 30 TeV. [Figure 29](#) (c), (d) present the limits obtained from the decay lengths of 10 – 100 meter. Here very low Yukawa couplings $\lesssim 10^{-8}$ are probed.

8 Conclusion

Type-III seesaw model is motivated to explain the tiny neutrino mass scale which predicts the heavy charged and neutral leptons. They mix with SM charged and neutral leptons via the Yukawa couplings and the vev of the SM Higgs doublet at the electroweak symmetry breaking scale. Current lower limit of this SU(2) triplet fermion obtained using the prompt

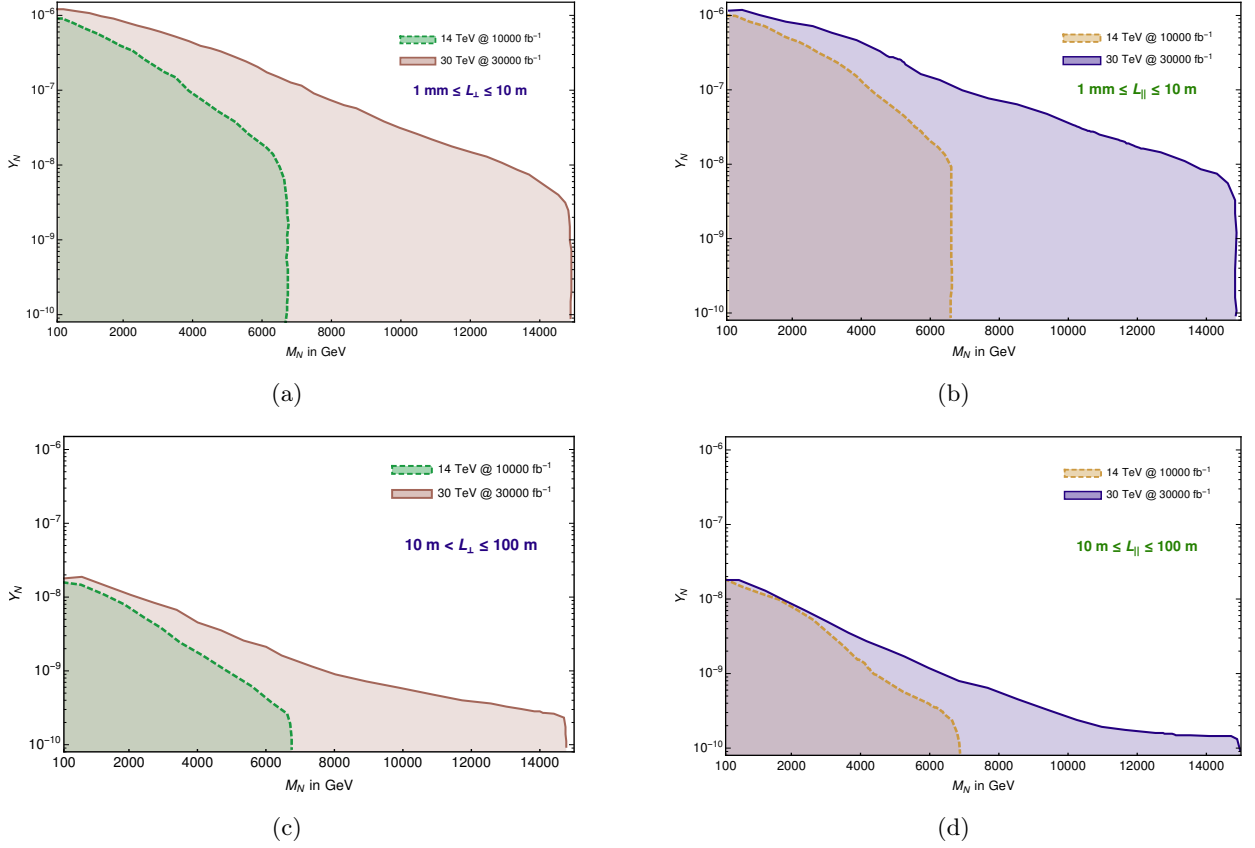


Figure 29. Limits obtained for Yukawa coupling versus Type-III fermion mass via transverse (a, c) and longitudinal (b, d) decay lengths for the finalstates containing atleast $2b$ -jets with the centre of mass energies of 14 and 30 TeV at the muon collider with integrated luminosities of 10000 and 30000 fb^{-1} , respectively. (a, b) represent $1 \text{ mm} \leq L_{\perp, \parallel} \leq 10 \text{ m}$ and (c, d) depict $10 \text{ m} \leq L_{\perp, \parallel} \leq 100 \text{ m}$ regions.

charged lepton finalstates is around 740 GeV [27–30] at 2σ with possible QCD corrections [72] but LHC with higher energy and luminosity can probe even higher mass range. The same Yukawa coupling also gives direct coupling to SM Higgs boson with the charged and neutral heavy fermions. Thus Higgs bosons can be produced from the decays of such heavy fermions proportional to the square of the Yukawa couplings. In particular, we focus on the parameter space with low Yukawa, where the displaced decays of N^\pm and N^0 occur.

In this article, we explored the displaced Higgs production from such decays both at the LHC/FCC and at the muon collider. The Higgs boson comes from these decays of $N^\pm \rightarrow h\ell^\pm$ and $N^0 \rightarrow h\nu$, where the former leads to the complete visible displaced finalstate for $Y_N \simeq 5 \times 10^{-7}$. Different Yukawa coupling ranges are probed, which are compatible with the atmospheric and the solar neutrino mass scale as well as very light ones which can be explored by the new detector, MATHUSLA. However, for lower Yukawa couplings i.e. $Y_N \leq 10^{-8}$ we observe two decay recoils: first from the decay of $N^\pm \rightarrow N^0\pi^\pm$ and the second one is from N^0 decays to the SM particles. We also notice that the longitudinal

boost at the LHC/FCC can lead to the enhancement of the displaced decay lengths, and thus has a better reach compared to the transverse one. The detailed analyses at the LHC with centre of mass energies of 14, 27 and 100 TeV are presented along with the bounds on Yukawa couplings and Type-III fermion masses. A very early data of 300fb^{-1} can probe Type-III fermion mass of ~ 4.3 TeV at the centre of mass energy of 100 TeV and higher luminosity LHC (HL-LHC) can probe mass range of 5.8 TeV with 3000fb^{-1} .

Displaced Higgs production in a supersymmetric Type-III seesaw mechanism is already looked into [31]. In general, the seesaw models with lower couplings predict displaced decays of right-handed neutrinos in case of Type-I seesaw [73, 74] but we do not expect any flying charged track in those scenarios. In case of Type-III seesaw at the LHC, N^\pm gives charged track before it decays, whereas N^0 has invisible track before the decay. Models with inert SU(2) triplet scalars also predicts displaced charged track but mostly leads to very soft leptons and jets due to phase space suppression induced by Z_2 symmetry [75, 76]. In a supersymmetric extension of such triplet scalar, the fermionic partners stay nearly degenerate at the tree-level as well as couple to SM fermions via the mixing with doublet like Higgsinos and gauginos, resulting displaced charged track along with large missing energy due to R -parity[77]. Thus, a demand of one visible and another invisible charged tracks, i.e. first and second recoils along with one(two) hard lepton(s) but not so large missing energy can segregate the scenario from others. The reconstruction of the Higgs bosons in this scenario, can distinguish it from other possible BSM scenarios having long-lived particles. In the context of supersymmetry and UED, where we see long lived particles often have larger missing energy in the finalstates, thus can also be easily segregated. In R -parity violating framework the displaced decays of the Higgs boson is studied in [78] though produced promptly.

Unlike at the LHC/FCC, at the muon collider, we can only produce N^+N^- , and thus two such displaced charged tracks will be visible before the recoil. At the muon collider, the mass ranges that can be probed is identical for both the transverse and the longitudinal modes due to fixed total momentum in each collision. However, one interesting fact we observe is that the transverse momentum of the N^\pm diverges perpendicular to the beam axis, as opposed to the LHC. This leads to higher momentum for transverse compared to longitudinal one, and predicts larger number of events for the transverse decay lengths. We plot the sensitivity regions in the Yukawa versus mass plane for two different decay length regions, i.e. 1 mm - 10 m and 10-100 m for the centre of mass energies of 14 and 30 TeV and it is evident that a detector with length around 10 m is sufficient in probing the larger ranges of the Yukawa coupling. Certainly, muon collider has good prospects in probing such scenarios having them in centre of mass frame and without initial state radiation.

Acknowledgements

PB acknowledges SERB CORE Grant CRG/2018/004971 and MATRICS Grant MTR/2020/000668 for the financial and computational support towards the work. CS would like to thank MOE Government of India for an JRF fellowship. PB and CS also thank Anirban Karan for some useful discussions. CS wishes to thank Antonio Costantini and Snehashis Parashar for some

useful discussions. PB wants to thank Kirtiman Ghosh for some crucial information regarding the simulation.

References

- [1] P.F. de Salas, D.V. Forero, S. Gariazzo, P. Martínez-Miravé, O. Mena, C.A. Ternes et al., *2020 global reassessment of the neutrino oscillation picture*, *JHEP* **02** (2021) 071 [[2006.11237](#)].
- [2] D.S. Hajdukovic, *On the absolute value of the neutrino mass*, *Mod. Phys. Lett. A* **26** (2011) 1555 [[1106.5810](#)].
- [3] R. Foot, H. Lew, X.G. He and G.C. Joshi, *Seesaw Neutrino Masses Induced by a Triplet of Leptons*, *Z. Phys. C* **44** (1989) 441.
- [4] B. Bajc and G. Senjanovic, *Seesaw at LHC*, *JHEP* **08** (2007) 014 [[hep-ph/0612029](#)].
- [5] R. Franceschini, T. Hambye and A. Strumia, *Type-III see-saw at LHC*, *Phys. Rev. D* **78** (2008) 033002 [[0805.1613](#)].
- [6] B. Bajc, M. Nemevsek and G. Senjanovic, *Probing seesaw at LHC*, *Phys. Rev. D* **76** (2007) 055011 [[hep-ph/0703080](#)].
- [7] E. Ma, *Pathways to naturally small neutrino masses*, *Phys. Rev. Lett.* **81** (1998) 1171 [[hep-ph/9805219](#)].
- [8] A. Arhrib, B. Bajc, D.K. Ghosh, T. Han, G.-Y. Huang, I. Puljak et al., *Collider Signatures for Heavy Lepton Triplet in Type I+III Seesaw*, *Phys. Rev. D* **82** (2010) 053004 [[0904.2390](#)].
- [9] P. Bandyopadhyay, S. Choubey and M. Mitra, *Two Higgs Doublet Type III Seesaw with mu-tau symmetry at LHC*, *JHEP* **10** (2009) 012 [[0906.5330](#)].
- [10] P. Bandyopadhyay, S. Choi, E.J. Chun and K. Min, *Probing Higgs bosons via the type III seesaw mechanism at the LHC*, *Phys. Rev. D* **85** (2012) 073013 [[1112.3080](#)].
- [11] O.J.P. Eboli, J. Gonzalez-Fraile and M.C. Gonzalez-Garcia, *Neutrino Masses at LHC: Minimal Lepton Flavour Violation in Type-III See-saw*, *JHEP* **12** (2011) 009 [[1108.0661](#)].
- [12] Y. Cai, T. Han, T. Li and R. Ruiz, *Lepton Number Violation: Seesaw Models and Their Collider Tests*, *Front. in Phys.* **6** (2018) 40 [[1711.02180](#)].
- [13] D. Goswami and P. Poulose, *Direct searches of Type III seesaw triplet fermions at high energy e^+e^- collider*, *Eur. Phys. J. C* **78** (2018) 42 [[1702.07215](#)].
- [14] F. del Aguila and J.A. Aguilar-Saavedra, *Electroweak scale seesaw and heavy Dirac neutrino signals at LHC*, *Phys. Lett. B* **672** (2009) 158 [[0809.2096](#)].
- [15] F. del Aguila and J.A. Aguilar-Saavedra, *Distinguishing seesaw models at LHC with multi-lepton signals*, *Nucl. Phys. B* **813** (2009) 22 [[0808.2468](#)].
- [16] P. Bandyopadhyay and A. Karan, *Probing Discerning Signatures of SM and Various Seesaw Models at e^-e^- Collider*, [2011.04191](#).
- [17] N.R. Agostinho, O.J.P. Eboli and M.C. Gonzalez-Garcia, *LHC Run I Bounds on Minimal Lepton Flavour Violation in Type-III See-saw: A Case Study*, *JHEP* **11** (2017) 118 [[1708.08456](#)].
- [18] D. Ibanez, S. Morisi and J.W.F. Valle, *Inverse tri-bimaximal type-III seesaw and lepton flavor violation*, *Phys. Rev. D* **80** (2009) 053015 [[0907.3109](#)].

- [19] A. Das and S. Mandal, *Bounds on the triplet fermions in type-III seesaw and implications for collider searches*, *Nucl. Phys. B* **966** (2021) 115374 [2006.04123].
- [20] S. Ashanujjaman and K. Ghosh, *Type-III see-saw: Phenomenological implications of the information lost in decoupling from high-energy to low-energy*, *Phys. Lett. B* **819** (2021) 136403 [2102.09536].
- [21] A. Das, S. Mandal and T. Modak, *Testing triplet fermions at the electron-positron and electron-proton colliders using fat jet signatures*, *Phys. Rev. D* **102** (2020) 033001 [2005.02267].
- [22] A. Abada, C. Biggio, F. Bonnet, M.B. Gavela and T. Hambye, *$\mu \rightarrow e$ gamma and $\tau \rightarrow l$ gamma decays in the fermion triplet seesaw model*, *Phys. Rev. D* **78** (2008) 033007 [0803.0481].
- [23] P. Escribano, J. Terol-Calvo and A. Vicente, *$(g - 2)_{e,\mu}$ in an extended inverse type-III seesaw model*, *Phys. Rev. D* **103** (2021) 115018 [2104.03705].
- [24] S. Jana, N. Okada and D. Raut, *Displaced Vertex and Disappearing Track Signatures in type-III Seesaw*, 1911.09037.
- [25] S. Goswami, K.N. Vishnudath and N. Khan, *Constraining the minimal type-III seesaw model with naturalness, lepton flavor violation, and electroweak vacuum stability*, *Phys. Rev. D* **99** (2019) 075012 [1810.11687].
- [26] P. Bandyopadhyay, S. Jangid and M. Mitra, *Scrutinizing Vacuum Stability in IDM with Type-III Inverse seesaw*, *JHEP* **02** (2021) 075 [2008.11956].
- [27] CMS collaboration, *Search for Evidence of the Type-III Seesaw Mechanism in Multilepton Final States in Proton-Proton Collisions at $\sqrt{s} = 13$ TeV*, *Phys. Rev. Lett.* **119** (2017) 221802 [1708.07962].
- [28] ATLAS collaboration, *Search for type-III seesaw heavy leptons in dilepton final states in pp collisions at $\sqrt{s} = 13$ TeV with the ATLAS detector*, *Eur. Phys. J. C* **81** (2021) 218 [2008.07949].
- [29] CMS collaboration, *Search for physics beyond the standard model in multilepton final states in proton-proton collisions at $\sqrt{s} = 13$ TeV*, *JHEP* **03** (2020) 051 [1911.04968].
- [30] C. Biggio, E. Fernandez-Martinez, M. Filaci, J. Hernandez-Garcia and J. Lopez-Pavon, *Global Bounds on the Type-III Seesaw*, *JHEP* **05** (2020) 022 [1911.11790].
- [31] P. Bandyopadhyay and E.J. Chun, *Displaced Higgs production in type III seesaw*, *JHEP* **11** (2010) 006 [1007.2281].
- [32] M. Cepeda et al., *Report from Working Group 2: Higgs Physics at the HL-LHC and HE-LHC*, *CERN Yellow Rep. Monogr.* **7** (2019) 221 [1902.00134].
- [33] MATHUSLA collaboration, *Explore the lifetime frontier with MATHUSLA*, *JINST* **15** (2020) C06026 [1901.04040].
- [34] J.P. Chou, D. Curtin and H.J. Lubatti, *New Detectors to Explore the Lifetime Frontier*, *Phys. Lett. B* **767** (2017) 29 [1606.06298].
- [35] D. Curtin et al., *Long-Lived Particles at the Energy Frontier: The MATHUSLA Physics Case*, *Rept. Prog. Phys.* **82** (2019) 116201 [1806.07396].
- [36] A. Coccaro, D. Curtin, H.J. Lubatti, H. Russell and J. Shelton, *Data-driven*

- Model-independent Searches for Long-lived Particles at the LHC*, *Phys. Rev. D* **94** (2016) 113003 [[1605.02742](#)].
- [37] R. Palmer et al., *Muon collider design*, *Nucl. Phys. B Proc. Suppl.* **51** (1996) 61 [[acc-phys/9604001](#)].
- [38] C.M. Ankenbrandt et al., *Status of muon collider research and development and future plans*, *Phys. Rev. ST Accel. Beams* **2** (1999) 081001 [[physics/9901022](#)].
- [39] J.P. Delahaye, M. Diemoz, K. Long, B. Mansoulié, N. Pastrone, L. Rivkin et al., *Muon Colliders*, [1901.06150](#).
- [40] N. Bartosik et al., *Preliminary Report on the Study of Beam-Induced Background Effects at a Muon Collider*, [1905.03725](#).
- [41] N. Bartosik et al., *Detector and Physics Performance at a Muon Collider*, *JINST* **15** (2020) P05001 [[2001.04431](#)].
- [42] H. Al Ali et al., *The Muon Smasher’s Guide*, [2103.14043](#).
- [43] A. Costantini, F. De Lillo, F. Maltoni, L. Mantani, O. Mattelaer, R. Ruiz et al., *Vector boson fusion at multi-TeV muon colliders*, *JHEP* **09** (2020) 080 [[2005.10289](#)].
- [44] D. Buttazzo, D. Redigolo, F. Sala and A. Tesi, *Fusing Vectors into Scalars at High Energy Lepton Colliders*, *JHEP* **11** (2018) 144 [[1807.04743](#)].
- [45] G.-y. Huang, F.S. Queiroz and W. Rodejohann, *Gauged $L_\mu-L_\tau$ at a muon collider*, *Phys. Rev. D* **103** (2021) 095005 [[2101.04956](#)].
- [46] G.-Y. Huang, S. Jana, F.S. Queiroz and W. Rodejohann, *Probing the $R_{K^{(*)}}$ Anomaly at a Muon Collider*, [2103.01617](#).
- [47] P. Asadi, R. Capdevilla, C. Cesarotti and S. Homiller, *Searching for Leptoquarks at Future Muon Colliders*, [2104.05720](#).
- [48] R. Capdevilla, D. Curtin, Y. Kahn and G. Krnjaic, *Discovering the physics of $(g-2)_\mu$ at future muon colliders*, *Phys. Rev. D* **103** (2021) 075028 [[2006.16277](#)].
- [49] K. Long, D. Lucchesi, M. Palmer, N. Pastrone, D. Schulte and V. Shiltsev, *Muon colliders to expand frontiers of particle physics*, *Nature Phys.* **17** (2021) 289 [[2007.15684](#)].
- [50] T. Han, D. Liu, I. Low and X. Wang, *Electroweak couplings of the Higgs boson at a multi-TeV muon collider*, *Phys. Rev. D* **103** (2021) 013002 [[2008.12204](#)].
- [51] T. Han, Z. Liu, L.-T. Wang and X. Wang, *WIMPs at High Energy Muon Colliders*, *Phys. Rev. D* **103** (2021) 075004 [[2009.11287](#)].
- [52] R. Capdevilla, D. Curtin, Y. Kahn and G. Krnjaic, *A No-Lose Theorem for Discovering the New Physics of $(g-2)_\mu$ at Muon Colliders*, [2101.10334](#).
- [53] T. Han, S. Li, S. Su, W. Su and Y. Wu, *Heavy Higgs Bosons in 2HDM at a Muon Collider*, [2102.08386](#).
- [54] P. Bandyopadhyay, A. Karan and R. Mandal, *Probing scalar leptoquarks at the colliders*, [To be appeared soon](#).
- [55] NNPDF collaboration, *Parton distributions for the LHC Run II*, *JHEP* **04** (2015) 040 [[1410.8849](#)].
- [56] M. Cirelli, N. Fornengo and A. Strumia, *Minimal dark matter*, *Nucl. Phys. B* **753** (2006) 178 [[hep-ph/0512090](#)].

- [57] P. Bandyopadhyay, E.J. Chun and C. Sen, *Displaced flavour violating leptonic jet signature at LHC and MATHUSLA*, [To be appeared soon](#).
- [58] T. Sjöstrand, S. Ask, J.R. Christiansen, R. Corke, N. Desai, P. Ilten et al., *An introduction to PYTHIA 8.2*, *Comput. Phys. Commun.* **191** (2015) 159 [[1410.3012](#)].
- [59] F. Staub, *SARAH 4 : A tool for (not only SUSY) model builders*, *Comput. Phys. Commun.* **185** (2014) 1773 [[1309.7223](#)].
- [60] A. Belyaev, N.D. Christensen and A. Pukhov, *CalcHEP 3.4 for collider physics within and beyond the Standard Model*, *Comput. Phys. Commun.* **184** (2013) 1729 [[1207.6082](#)].
- [61] CMS collaboration, *Search for heavy bottom-like quarks in 4.9 inverse femtobarns of pp collisions at $\sqrt{s} = 7$ TeV*, *JHEP* **05** (2012) 123 [[1204.1088](#)].
- [62] CMS collaboration, *Identification of heavy-flavour jets with the CMS detector in pp collisions at 13 TeV*, *JINST* **13** (2018) P05011 [[1712.07158](#)].
- [63] CMS collaboration, *CMS technical design report, volume II: Physics performance*, *J. Phys. G* **34** (2007) 995.
- [64] ATLAS collaboration, *ATLAS detector and physics performance: Technical Design Report, 1*, .
- [65] D.R. Tovey, *Transverse mass and invariant mass observables for measuring the mass of a semi-invisibly decaying heavy particle*, *JHEP* **11** (2010) 148 [[1008.3837](#)].
- [66] P. Bandyopadhyay, S. Dutta, M. Jakkapu and A. Karan, *Exploring spins of beyond Standard Models via angular distribution at the LHC*, [2007.12997](#).
- [67] S. Chakraborty, M. Mitra and S. Shil, *Fat Jet Signature of a Heavy Neutrino at Lepton Collider*, *Phys. Rev. D* **100** (2019) 015012 [[1810.08970](#)].
- [68] A. Bhardwaj, A. Das, P. Konar and A. Thalapillil, *Looking for Minimal Inverse Seesaw scenarios at the LHC with Jet Substructure Techniques*, *J. Phys. G* **47** (2020) 075002 [[1801.00797](#)].
- [69] P. Bandyopadhyay and B. Bhattacharjee, *Boosted top quarks in supersymmetric cascade decays at the LHC*, *Phys. Rev. D* **84** (2011) 035020 [[1012.5289](#)].
- [70] PARTICLE DATA GROUP collaboration, *Review of Particle Physics*, *PTEP* **2020** (2020) 083C01.
- [71] G.C. (RHUL), “Statistics (40).” <https://pdg.lbl.gov/2017/reviews/rpp2017-rev-statistics.pdf>, September, 2017.
- [72] R. Ruiz, *QCD Corrections to Pair Production of Type III Seesaw Leptons at Hadron Colliders*, *JHEP* **12** (2015) 165 [[1509.05416](#)].
- [73] P. Bandyopadhyay, E.J. Chun and J.-C. Park, *Right-handed sneutrino dark matter in $U(1)'$ seesaw models and its signatures at the LHC*, *JHEP* **06** (2011) 129 [[1105.1652](#)].
- [74] P. Bandyopadhyay, *Displaced lepton flavour violating signatures of right-handed sneutrinos in $U(1)'$ supersymmetric models*, *JHEP* **09** (2017) 052 [[1511.03842](#)].
- [75] S. Jangid and P. Bandyopadhyay, *Distinguishing Inert Higgs Doublet and Inert Triplet Scenarios*, *Eur. Phys. J. C* **80** (2020) 715 [[2003.11821](#)].
- [76] P. Bandyopadhyay and A. Costantini, *Obscure Higgs boson at Colliders*, *Phys. Rev. D* **103** (2021) 015025 [[2010.02597](#)].

- [77] A. Sabancı Keceli, P. Bandyopadhyay and K. Huitu, *Long-lived triplinos and displaced lepton signals at the LHC*, *Eur. Phys. J. C* **79** (2019) 345 [[1810.09172](#)].
- [78] P. Bandyopadhyay, P. Ghosh and S. Roy, *Unusual Higgs boson signal in R-parity violating nonminimal supersymmetric models at the LHC*, *Phys. Rev. D* **84** (2011) 115022 [[1012.5762](#)].